RESEARCH FRONT

CSIRO PUBLISHING

Marine and Freshwater Research, 2020, **71**, 355–373
https://doi.org/10.1071/MF19200

Some observations on the biogeochemical cycling of zinc in the Australian sector of the Southern Ocean: a dedication to Keith Hunter

Michael J. Ellwood[A], *Robert Strzepek*[B], *Xiaoyu Chen*[A], *Thomas W. Trull*[C] *and Philip W. Boyd*[B]

[A]Research School of Earth Sciences, Australian National University, Canberra, ACT 2601, Australia.
[B]Institute for Marine and Antarctic Studies, University of Tasmania, Hobart, Tas. 7004, Australia.
[C]CSIRO Oceans and Atmosphere, Hobart, Tas. 7004, Australia.
[D]Corresponding author. Email: michael.ellwood@anu.edu.au

Abstract. In this study we investigated the distribution of dissolved and particulate zinc (dZn and pZn respectively) and its isotopes in the Subantarctic Zone as part of a Geotraces Process voyage. dZn and pZn depth profiles contrasted each other, with dZn showing depletion within the euphotic zone while pZn profiles showed enrichment. Fitting a power law equation to the pZn profiles produced an attenuation factor of 0.82, which contrasted values for particulate phosphorus, cadmium and copper. The results indicate that zinc has a longer regeneration length scale than phosphorus and cadmium, but shorter than copper. The differential regeneration of pZn relative to that of particulate phosphorus likely explains why dZn appears to have a deeper regeneration profile than that of phosphate. The dZn isotope ($\delta^{66}Zn_{dissolved}$) profiles collected across the Subantarctic Zone showed differing profile structures. For one station collected within an isolated cold-core eddy (CCE), $\delta^{66}Zn_{dissolved}$ showed surface enrichment relative to deep waters. The corresponding pZn isotope profiles within the CCE did not show enrichment; rather, they were subtly depleted in surface waters and then converged to similar values at depth. Zinc isotope fractionation can be explained through a combination of fractionation processes associated with uptake by phytoplankton, zinc complexation by natural organic ligands and zinc regeneration from particulate matter.

Received 30 May 2019, accepted 7 September 2019, published online 3 December 2019

Introduction

Zinc is an essential micronutrient for phytoplankton because it is involved in several key enzyme reactions within cells. The oceanic distribution of zinc is similar to that of silicic acid, which has puzzled researchers for many years (Bruland *et al.* 1978; Hunter and Boyd 1999). Recent modelling efforts suggest that the coupling of these two nutrients may result from: (1) physical circulation within the Southern Ocean and biogeochemical modification of these waters by diatoms (Vance *et al.* 2017; de Souza *et al.* 2018); and (2) biological uptake in the Southern Ocean coupled with the reversible scavenging of zinc onto sinking particles (Roshan *et al.* 2018; Weber *et al.* 2018). These modelling studies rely heavily on the concentration and isotope composition of zinc in the dissolved phase. Further, in all these modelling scenarios, the Southern Ocean is critical in determining the initial biogeochemical status of zinc, silicic acid and phosphate in surface and subsurface waters, which is then propagated globally by mode and intermediate water masses (Sarmiento *et al.* 2004).

The Subantarctic Zone (SAZ) of the Southern Ocean represents ~50% of the total area of the Southern Ocean and is an important contributor to the export of nutrients from the Southern Ocean into the global ocean thermocline. The SAZ is bound by the Subtropical Front (STF) to the north and the Subantarctic Front (SAF) and the Polar Front (PF) to the south (Fig. 1). The SAZ is a major contributor to oceanic uptake of CO_2, with an annual flux >1 Gt C $year^{-1}$ (Metzl *et al.* 1999; Frölicher *et al.* 2015). Although primary production within the SAZ makes a major contribution to global CO_2 uptake, primary production in SAZ waters is limited by silica, iron and light availability (Boyd *et al.* 1999; Hutchins *et al.* 2001; Petrou *et al.* 2011; Westwood *et al.* 2011). In SAZ surface waters, silicic acid concentrations typically range between ~0.5 and 3 μM (Lourey and Trull 2001), which are on the cusp of being growth limiting (Paasche 1973; Franck *et al.* 2005).

To date, there have only been a handful of studies looking at zinc cycling in the SAZ. Work by Ellwood (2008), Samanta *et al.* (2017) and Butler *et al.* (2013) for the south-west Pacific sector of the Southern Ocean all showed depletion of zinc and silicic in surface waters, with concentrations ranging between 0.06 and 0.36 nmol kg^{-1}. Although these zinc concentrations are low, there is little evidence to suggest that they are low enough to limit phytoplankton growth (Ellwood 2004; Butler *et al.* 2013). Understanding the processes that affect the cycling of zinc in the

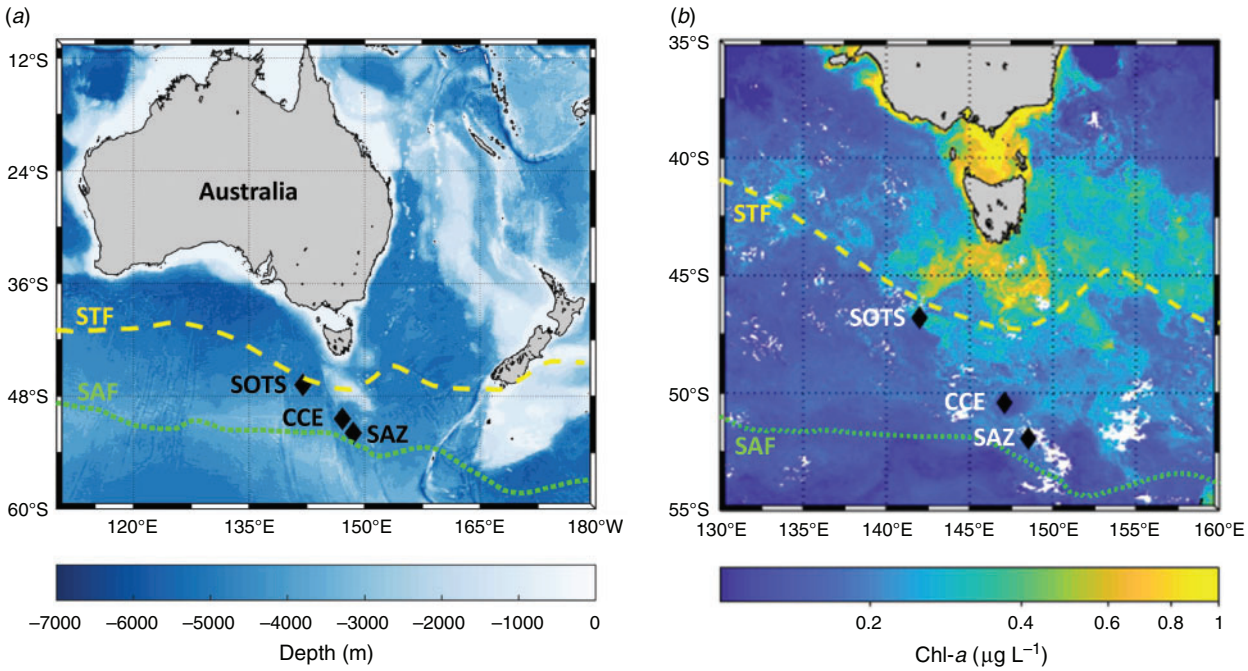

Fig. 1. (*a*) Bathymetry map showing the locations of the Cold Core Eddy (CCE), Subantarctic Zone (SAZ) and Southern Ocean Time Series (SOTS) stations. The positions of the Subtropical Front (STF) and the Subantarctic Front (SAF) are also drawn based on data from Orsi *et al.* (1995). (*b*) Satellite-derived chlorophyll (Chl)-*a* concentrations for March 2016. Maps were drawn using M_map (ver. 1.4k, R. Pawlowicz, see www.eoas.ubc.ca/~rich/map.html).

SAZ is important because this region is where Subantarctic Mode Water (SAMW) forms and ventilates lower latitudes (Sarmiento *et al.* 2004; Sallée *et al.* 2006).

To date, little work has looked at zinc isotope cycling between the dissolved and particulate phases (dZn and pZn respectively). The aim of the work presented here was to understand the cycling of dZn and pZn in the subantarctic waters south of Australia. This work forms part of the international GEOTRACES program.

Materials and methods

Sampling sites

The Southern Ocean Time Series (SOTS) site is located at 47°S, 142°E, south-west of Tasmania, Australia (Fig. 1). This has been a long-term mooring site where biophysicochemical water column measurements have been made since 1998 and it presently forms part of the Australian Integrated Marine Observing System (IMOS). The SOTS site is located on the northern edge of the SAZ, with typical sea surface temperatures ranging between ~9 and 13°C (Fig. 1; Herraiz-Borreguero and Rintoul 2011). The site is in deep water (>4500 m) and is located on the western side of the Tasman Rise. Although the site is located on the northern edge of the SAZ, upper ocean oceanography at the site can be complex. The oceanographic properties of the site are generally representative of the Australian sector of the SAZ, but the site is also affected by Tasman Sea Outflow water, which forms part of the return flow to the South Pacific super gyre (Ridgway 2007; Oliver and Holbrook 2014). This westward-flowing water exhibits some properties of subtropical water sourced from the Tasman Sea, but is also affected by eddy circulation near Tasmania that is associated with the westward leakage of the East Australia Current (Weeding and Trull 2014; Shadwick *et al.* 2015). For the present study, the SOTS site was occupied between 18 and 21 March 2016 and again between 19 and 27 March 2017.

The cyclonic cold-core eddy (CCE) site was studied between 28 March and 3 April 2016 (Fig. 1), with its centre located at ~50.4°S, 147.1°E. The eddy was ~190 km in diameter and was a stable feature that had formed in mid-February 2016, ~1.2° further south of the sampling site near the SAF (Moreau *et al.* 2017). After formation, the eddy moved slowly northward across the northern extension of the SAF with a rotation speed of 0.527 rad day^{-1} (Moreau *et al.* 2017; Patel *et al.* 2019). The biogeochemical properties of this eddy differ from external waters (Moreau *et al.* 2017; Patel *et al.* 2019). Because this eddy became 'structurally closed' after development, its ability to entrain and detrain nutrients, dissolved iron, phytoplankton and zooplankton was restricted. That is, it behaved much like a static mesocosm.

The other site of interest was located at 51.90°S, 148.51°E within the SAZ and was designated as the 'SAZ' site (Fig. 1). It was located north of the northern extension of the SAF and is regarded as having biogeochemical properties typical of the SAZ. The site was sampled between 7 and 11 April 2016.

Equipment cleaning

All equipment used in this study had been extensively acid cleaned. Typically, sample bottles were soaked for 1 week in 15% aqua regia ($HCl : HNO_3$ 3 : 1) reagent grade, rinsed and

then soaked for 1 further week in 2% HNO_3. Water used to rinse bottles was purified using a water purification system (Millipore, Melbourne, Vic., Australia). The final step in the process was to fill bottles with 0.5% (w/w) Teflon-distilled (designated here as 't-acid'; Savillex, Minneapolis, MN, USA) HNO_3 (Mattinson 1972) and then double-bag them. Laboratory plasticware was acid cleaned by heating in aqua regia followed by heating with 0.5% t-HNO_3.

Conductivity, temperature and depth and nutrient sampling

Conductivity, temperature and depth (CTD) profile data and water samples for nutrient and biological parameters were collected with a winch-lowered package consisting of an SBE 911plus CTD (Seabird, Seattle, WA, USA), a Turner Designs (San Jose, CA, USA) fluorometer and a 24-bottle SBE 32 Carousel water sampler (Seabird). Salinities were standardised to standard seawater (Ocean Scientific International Ltd, Portsmouth, UK). Samples for macronutrients, phosphate, nitrate, nitrite, ammonia and silicic acid were collected and analysed at sea on unfiltered samples using a Seal AA3 segmented flow system (Seal Analytical, Mequon, WI, USA) following the procedures outlined by Armstrong *et al.* (1967) and Wood *et al.* (1967). Horizontal CTD profile measurements of the water column were made using a towed undulating (0–200 m) SBE 911plus CTD system (TRIAXUS; MacArtney, Esbjerg, Denmark).

Primary production measurements

Net primary production (i.e. ^{14}C uptake rates) were determined for water column samples collected at six depths from 0 to 100 m (Boyd *et al.* 2005). These measurements involved spiking samples with radioactive carbon ($NaH^{14}CO_3$) and incubating them for 24 h. The light conditions for the six collection depths were simulated using neutral density screening for each incubator chamber. After 24 h, samples were filtered, rinsed reducing titanium solution to remove extracellular ^{14}C and archived for scintillation counting ashore.

Trace metal sampling

Seawater samples for trace metal and isotope determination were collected using acid-cleaned, Teflon-coated, externally sprung 12-L Niskin bottles attached to an autonomous rosette (Seabird) equipped with an SBE 911plus CTD unit (Seabird). Upon retrieval, the Niskin bottles were transferred to a clean container laboratory. Seawater samples for dissolved trace metal analysis were filtered through acid-cleaned, 0.2-μm capsule filters (Supor AcroPak 200; Pall, New York, NY, USA) and acidified with t-HNO_3 to a final pH of ≤1.8. The sampling protocols followed recommendations in the GEOTRACES Cruise and Methods Manual (Cookbook) (http://www.geotraces.org/science/intercalibration/222-sampling-and-sample-handling-protocols-for-geotraces-cruises, accessed 10 November 2015).

Particulate trace metal samples were collected *in situ* onto acid-leached 0.2-μm Supor (142-mm diameter) filters (Pall) using six large-volume dual-head pumps (McLane Research Laboratories, East Falmouth, MA, USA), deployed at various water depths. For most profiles, one pump depth was used as a blank check whereby only 4–8 L of water was pumped through the filter.

Trace metal analysis

Purification and separation of zinc from the seawater matrix was performed by solid-phase extraction using chelating ion chromatography followed by anion exchange chromatography (Samanta *et al.* 2016, 2017). For dZn isotope ($\delta^{66}Zn_{dissolved}$) determination, seawater samples (2 L) were spiked with a ^{67}Zn–^{68}Zn double spike (3–6 : 1 spike : sample ratio; Samanta *et al.* 2016, 2017). Samples were left overnight to equilibrate and then preconcentrated at a pH of 4.5 by passing them over 0.5-mL columns packed with Nobias PA Chelate PA1L resin (Hitachi-Hitech, Tokyo, Japan) at a flow rate of 2 mL min^{-1}. Samples were rinsed with 4 mL of ammonium acetate buffer solution (1% w/w) followed by elution with 4 mL of 1 M t-HNO_3. Samples were evaporated to dryness and redissolved with 0.5 mL of 6 M t-HCl. Samples were further purified using the anion exchange procedure described by Poitrasson and Freydier (2005). This procedure involved loading samples onto ~200-μL columns filled with cleaned AG-MP1 resin (Bio-Rad, Sydney, NSW, Australia). Salts and other elements not of interest were eluted from columns by passing 3 × 1 mL of 6 M t-HCl followed by 3 × 1 mL of 0.5 M t-HCl. This fraction was saved for iron isotope analysis. Zinc was eluted from each column by passing 3 × 1 mL of 0.5 M t-HNO_3 over the AG-MP1 resin. The collected zinc samples were evaporated to dryness and redissolved in 2% (w/w) HNO_3.

Particulate samples for trace element and $\delta^{66}Zn$ determination were thawed and processed using the acid digestion protocol of Eggimann and Betzer (1976), as described by Ellwood *et al.* (2015).

Zinc isotopes were determined using a NeptunePlus multi-collector ICPMS (ThermoScientific, Sydney, NSW, Australia) with an APEX-IR introduction system (ESI, Omaha, NB, USA) and with X-type skimmer cones. At the start of each measurement session, the instrument was tuned for intensities on mass ^{62}Ni, ^{63}Cu, ^{65}Cu, ^{64}Zn, ^{66}Zn, ^{67}Zn and ^{68}Zn. Samples were analysed in medium resolution mode in groups of three, bracketed with the IRMM-3702 standard (Institute for Reference Materials and Measurements, Geel, Belgium). A 2% (v/v) HNO_3 blank measurement was made before each sample or standard measurement. All measurements were made as one block of 45 cycles with a 4-s integration time. On-peak blank correction of sample isotope intensities was undertaken by subtracting the average intensity of the 45 cycle measurements for each of the measured isotopes from the isotope intensities measured for each blank.

All zinc isotope measurements were collected relative to the standard reference material IRMM-3702, which is isotopically indistinguishable from the new zinc standard 'AA-ETH Zn' (Archer *et al.* 2017). The IRMM-3702 standard is offset by 0.30 ± 0.05‰ (s.d) with respect to the Johnson Matthey (JMC) Lyon standard (Cloquet *et al.* 2008; Moeller *et al.* 2012; Archer *et al.* 2017). Zinc isotope values were subsequently related to the JMC Lyon standard by adding 0.30‰ to all our results. Thus, the $\delta^{66}Zn$ values are reported using the following equation:

$$\delta^{66}Zn_{JMC_{Lyon}} = \left(\frac{\delta^{66}Zn/\delta^{64}Zn_{sample}}{\delta^{66}Zn/\delta^{64}Zn_{IRMM_{3702}}}\right) \times 1000 + 0.3 \quad (1)$$

Zinc isotope reproducibility was tested by processing an in-house seawater standard multiple times. This standard was

collected at a depth of 3500 m during the PINTS ('Primary productivity induced by Iron and Nitrogen in the Tasman Sea') campaign in 2010 from Station P3 (Hassler *et al.* 2014). Full processing of the sample produced a mean (±2 s.d.) $\delta^{66}Zn_{JMCLyon}$ value of 0.63 ± 0.02 ($n = 3$), which is isotopically indistinguishable from the mean (±2 s.d.) value of 0.60 ± 0.05 ($n = 6$) obtained by Samanta *et al.* (2017; Table 1).

Elemental analysis for dissolved and particulate copper, cadmium, nickel, manganese, aluminium and phosphorus was made by removing aliquots from preconcentrated digests destined for zinc isotope analysis. These were measured by high-resolution inductively coupled plasma–mass spectrometry (ICP-MS; Element XR; ThermoScientific) in medium resolution mode. Iron concentrations were obtained from iron isotope analysis (M. J. Ellwood, unpubl. data). Blanks associated with the collection and processing of particulate samples are given in Tables 1 and 2, along with results for the analysis of an in-house standard for dissolved trace metals. Overall, the dissolved results produced in this study are comparable to the results obtained by Samanta *et al.* (2017) for zinc, Thompson and Ellwood (2014) for copper and previous measurements made at the Australian National University for iron and nickel in 2011.

One-dimensional biogeochemical modelling

The potential processes that affect the distribution of dZn relative to that of nitrate or phosphate and phytoplankton biomass were explored using a one-dimensional (1-D) model (Fig. 2). During the development of the model, we were mindful that some processes, (e.g. lateral advection) are not parameterised by the model. Some of the biological processes parameterised within the model are also simplified. The rationale for using this 1-D model is to explore the relative effect (and interplay) that processes such as phytoplankton utilisation of zinc, zinc complexation to natural organic ligands and regeneration have on dZn and pZn isotope profiles. One should be mindful that this model is not three-dimensional in nature and only extends to 500 m (i.e. it lacks the ability to simulate the global processes). That said, this 1-D model is a useful tool for exploring processes that influence the cycling of zinc within the CCE.

The 1-D model is based on the model developed by Schlosser *et al.* (2014) and includes one phytoplankton group and references key nutrients, including nitrate, phosphate, zinc and iron (Fig. 2). Note that the model has an iron component, which will not be presented in this paper. The model includes mixing, which supplies nutrients into the euphotic zone and the main loss process for nutrients and zinc from the euphotic zone (organic matter export; Fig. 2). The zinc component within the model also includes complexation to natural organic ligands. In the model presented, scavenging of zinc from solution and isotope fractionation associated with this potential process are considered in a limited number of runs (John and Conway 2014; Weber *et al.* 2018). We justify this because our model focuses on the upper water column where zinc predominantly complexes to natural organic ligands, which will tend to reduce the free Zn^{2+} concentration such that scavenging would be a minor component of its overall cycling in the upper water column.

As mentioned, the model does not include advection, which is justifiable for several reasons: (1) vertical advection (i.e. upwelling) occurs in the Southern Ocean primarily south of the PF and not in the SAZ and SAF regions examined here (Speer *et al.* 2000); (2) zonal advection brings in waters with similar properties from upstream in the Antarctic Circumpolar Current (Trull *et al.* 2001*b*), and can thus be ignored; and (3) meridional transport is dominated by northward Ekman transport, and although this does supply nutrients over the annual mean, in late summer surface concentrations between the SAF and PF zone are very uniform (Trull *et al.* 2001*a*), so this term can also be ignored.

In the model, phytoplankton production (γ_{phyto}) is expressed as a function of nitrogen biomass. The limiting term (i.e. the minimum, min) for γ_{phyto} is expressed as follows (the definitions for all symbols and their values are given in Table 3):

$$\gamma_{phyto} = \min\left[\frac{[N]}{k_{phyto.N} + [N]}, \frac{[P]}{k_{phyto.P} + [P]}, \frac{[PAR]}{k_{phyto.PAR} + [PAR]}\right] \quad (2)$$

In the upper water column, at and above the depth of peak biomass (i.e. the deep chlorophyll maximum), the regeneration of nutrients back into solution is expressed as a linear function relative to biomass. Below this depth the rate of nutrient regeneration decreases following the Martin particulate organic carbon (POC) attenuation expression power law (Martin *et al.* 1987):

$$k_{regen.z} = k_{regen.z_0}(z/z_0)^b \quad (3)$$

where z is depth with respect to z_0, which was set to depth below the peak in biomass. This function effectively trends the sinking particles as transitioning from fresh to refractory with depth. For simplicity, the model used single values of k_{regen} (0.35 day^{-1}) and the power law exponent b (0.858; Martin *et al.* 1987) for all components. As shown in the results, it is likely that b varies among elements, and the ramifications of choosing a single value are explored in the Discussion.

For dissolved inorganic nitrogen (NO_3), Eqn 4 and 5 express its uptake by phytoplankton, its exchange between boxes above (j) and below ($j-2$) and its regeneration from phytoplankton (expressed here as particulate organic nitrogen, PON):

$$\frac{d[NO_3]_{j-1}}{dt} = k_{mix} \cdot ([NO_3]_j + [NO_3]_{j-2}) - 2 \cdot k_{mix} \cdot [NO_3]_{j-1} + k_{regen} \cdot [PON]_{j-1} - \gamma_{phyto} \cdot \mu_{max.phyto} \cdot [NO_3]_{j-1} \quad (4)$$

Note that the maximum uptake rate $\mu_{max.phyto}$ is in units of nitrogen here, and thus scaling to the observed ^{14}C uptake rates requires adjustment by the Redfield C : N ratio.

Overall, the change in PON can be expressed as follows:

$$\frac{d[PON]_{j-1}}{dt} = \gamma_{phyto} \cdot \mu_{max.phyto} \cdot [NO_3]_{j-1} + k_{sink} \cdot [PON]_j - k_{sink} \cdot [PON]_{j-1} \pm k_{regen} \cdot [PON]_j \quad (5)$$

In this expression (Eqn 5), and for the other particle expressions (Eqn 7, 11; see below), the mixing terms do not appear

Table 1. Dissolved trace metal and zinc isotope dataset for samples collected in 2016 and 2017 at the Cold Core Eddy station, the Subantarctic Zone station and at the Southern Ocean Time Series station

Values for $\delta^{66}Zn$ are given as the mean ± 2 s.e. for each measurement. Blanks ($n = 5$) are based on a 2-L sample being processed. For 'previous' measurements, most are unpublished and represent measurements made in 2011 for a large volume sample collected from 3500 m at Station P3 during the PINTS expedition (Hassler *et al.* 2014). Station P3 was located at 46°S, 160°E in the South Tasman Sea. ND, not determined

Depth (db)	Fe (nmol kg^{-1})	Zn (nmol kg^{-1})	$\delta^{66}Zn$ (‰)	Al (nmol kg^{-1})	Ni (nmol kg^{-1})	Cu (nmol kg^{-1})	Mn (nmol kg^{-1})	Cd (nmol kg^{-1})	NO_3 (μM)	PO_4 (μM)	Si (μM)	NH_4 (μM)	NO_2 (μM)
Cold Core Eddy													
15	0.024	0.3	0.93 ± 0.04	0.14	5.41	0.86	0.17	360	22.2	1.56	3.3	0.32	0.28
40	0.022	0.42	0.67 ± 0.03	0.12	5.37	0.86	0.18	375	22.2	1.56	3.3	0.32	0.28
70	0.018	0.46	0.64 ± 0.03	0.09	5.65	0.9	0.19	384	22.4	1.58	3.4	0.38	0.28
100	0.028	0.63	0.42 ± 0.03	0.27	5.35	0.89	0.2	443	23.3	1.67	3.6	0.81	0.3
150	0.027	0.98	0.50 ± 0.04	0.08	5.69	0.94	0.24	543	24.4	1.74	6.5	0.59	0.55
200	0.033	1.21	0.33 ± 0.03	0.17	5.46	0.98	0.23	580	25.7	1.79	9.7	0.21	0.07
300	0.41	0.9	0.38 ± 0.03	0.67	5.7	0.94	0.24	597	26.6	1.84	14.2	0.15	0.01
750	0.71	3.17	0.57 ± 0.04	1.18	6.49	1.27	0.18	860	33.2	2.31	41.6	0.09	0.01
1000	0.51	3.8	0.43 ± 0.04	0.53	6.57	1.33	0.15	899	34.7	2.42	58.2	0.09	0.01
1250	0.52	4.2	0.47 ± 0.04	0.5	6.87	1.53	0.17	881	34.8	2.42	68.8	0.06	0.01
1500	0.37	5.06	0.49 ± 0.03	0.36	6.69	1.56	0.21	873	33.9	2.36	76	0.03	0.01
Subantarctic Zone station													
15	0.06	0.37	0.43 ± 0.04	0.09	4.26	0.77	0.17	111	14.5	1.11	1.3	0.24	0.28
40	0.036	0.24	0.45 ± 0.05	0.1	4.22	0.61	0.18	112	14.5	1.11	1.3	0.23	0.28
70	0.047	0.21	0.54 ± 0.06	0.09	4.13	0.6	0.16	107	14.5	1.11	1.3	0.27	0.28
100	0.035	0.26	0.47 ± 0.06	0.11	4.44	0.65	0.23	232	14.4	1.1	1.4	0.23	0.28
150	0.046	0.35	0.42 ± 0.05	0.15	4.23	0.61	0.15	240	15.7	1.17	3	0.1	0.07
200	0.068	0.45	0.41 ± 0.06	0.1	4.44	0.67	0.22	234	15.6	1.15	3.9	0.14	0.01
300	0.87	0.5	0.49 ± 0.07	0.19	4.56	0.67	0.15	298	16.4	1.21	4.4	0.12	0.01
500	0.13	0.56	0.51 ± 0.07	0.22	5.12	0.79	0.06	526	18.6	1.35	5.7	0.14	0.01
750	0.30	1.5	0.49 ± 0.05	0.23	5.52	0.87	0.13	622	26.2	1.83	16	0.13	0
1000	0.35	2.45	0.44 ± 0.03	0.2	5.78	0.95	0.07	674	31	2.17	30.5	0.12	0
1250	0.41	3.75	0.39 ± 0.04	0.19	6.66	1.16	0.07	807	33.8	2.38	49.6	0.12	0
1500	0.44	4.74	0.50 ± 0.03	0.17	6.79	1.28	0.05	821	34.9	2.46	66	0.08	0
Southern Ocean Time Series													
Station 2016													
15	0.063	0.42	0.25 ± 0.04	ND	ND	ND	ND	ND	4.5	0.46	1.3	0.19	0.17
40	0.057	0.25	0.33 ± 0.07	0.27	3.17	0.37	0.3	7	4.6	0.46	1.3	0.17	0.17
70	0.064	0.26	0.33 ± 0.05	0.26	3.1	0.37	0.37	5	4.9	0.48	1.3	0.19	0.18
100	0.21	0.42	0.32 ± 0.04	0.62	2.76	0.4	0.36	65	10.7	0.81	3.5	0.02	0.03
150	0.19	0.45	0.26 ± 0.06	0.55	3.15	0.41	0.41	58	12.3	0.91	4.1	0	0.01
200	0.21	0.33	0.32 ± 0.07	0.55	3.39	0.46	0.43	89	13.5	0.98	4.6	0.03	0.01
300	0.19	0.51	0.21 ± 0.08	0.5	3.59	0.53	0.35	130	14.9	1.08	5.1	0.04	0.01
500	0.22	0.42	0.32 ± 0.11	0.43	3.77	0.55	0.33	186	16.7	1.2	5.8	0.05	0.02
750	0.50	1.14	0.35 ± 0.05	0.64	4.17	0.59	0.19	224	23.5	1.62	13.6	0.02	0
1000	0.57	2.14	0.36 ± 0.05	0.57	5.71	0.86	0.09	567	29	2	28.5	0.02	0.01
1250	0.53	3.43	0.42 ± 0.04	0.33	7.16	0.98	0.08	682	33.3	2.3	48.6	0.03	0
1500	0.56	4.92	0.43 ± 0.04	0.43	7.02	1.45	0.11	714	35	2.43	70.6	0.01	0
Station 2017													
15	0.16	0.4	ND	0.73	2.21	0.8	0.24	18	6.5	0.57	0.2	0.15	0.31
40	0.18	0.55	ND	0.38	2.01	0.33	0.25	14	7.2	0.61	0.2	0.13	0.3

(*Continued*)

Table 1. (Continued)

Depth (db)	Fe (nmol kg^{-1})	Zn (nmol kg^{-1})	δ^{66}Zn (‰)	Al (nmol kg^{-1})	Ni (nmol kg^{-1})	Cu (nmol kg^{-1})	Mn (nmol kg^{-1})	Cd (nmol kg^{-1})	NO_3 (μM)	PO_4 (μM)	Si (μM)	NH_4 (μM)	NO_2 (μM)
70	0.15	0.37	ND	0.38	2.16	0.45	0.29	16	9.5	0.77	0.8	0.22	0.52
100	0.17	0.36	ND	0.58	3.2	0.44	0.36	28	10.2	0.75	2.5	0.04	0
150	0.32	0.54	ND	2.13	3.24	0.46	0.39	127	13.4	0.95	3.9	0.02	0
200	0.24	0.5	ND	0.79	3.47	0.56	0.38	171	14.5	1.03	3.6	0.02	0.01
300	0.21	0.51	ND	0.56	3.73	0.65	0.33	178	15	1.06	3.8	0.02	0
500	0.24	0.75	ND	0.72	3.71	0.55	0.31	191	16.3	1.15	4.2	0.02	0
750	0.40	0.94	ND	1.02	3.95	0.59	0.3	291	23.5	1.59	11.9	0.01	0
1000	0.33	2.1	ND	0.92	5.08	0.81	0.31	552	29.3	1.97	23.5	0.01	0
1250	0.39	3.46	ND	0.92	5.63	0.98	0.31	683	33.1	2.25	44.6	0.01	0
1450	0.42	4.72	ND	0.73	6.13	1.26	0.21	737	34.8	2.38	61.6	0	0
Blanks	0.004[A]	0.012		0.034	0.019	0.019	0.007	6					
In-house standard ($n = 3$)	0.66 ± 0.01	6.84 ± 0.09	0.625 ± 0.022[B]	0.63 ± 0.21	6.93 ± 0.30	3.08 ± 0.15	0.034 ± 0.026	814 ± 37					
Previous measurements	0.57	6.24 ± 0.02[B]	0.60 ± 0.02[C]	ND	7.31	3.03[B]	ND	841					

[A]Based on a 0.4-ng iron isotope method blank scaled to 2 L.
[B]Data are given as the mean ± 2 s.d. ($n = 3$).
[C]Published results for zinc (Samanta *et al.* 2017) and copper (Thompson and Ellwood 2014).

Table 2. Particulate trace metal and zinc isotope dataset for samples collected in 2016 and 2017 at the Cold Core Eddy (CCE) station, the Subantarctic Zone (SAZ) station and at the Southern Ocean Time Series (SOTS) station

Note multiple casts are presented for the CCE and SOTS stations. Values for δ^{66}Zn are given as the mean ± 2 s.e. for each measurement. Blanks ($n = 3$) are based filter blanks scaled to the volume of water filtered. ND, not determined

Depth (m)	Zn (pM)	δ^{66}Zn (‰)	Cu (pM)	Cd (pM)	P (nM)
CCE station					
Profile 1					
40	33	0.29 ± 0.04	23.3	7.6	13
90	39	0.29 ± 0.04	34	10.7	19.5
150	12	0.32 ± 0.04	13.2	1.7	2.9
250	12	0.44 ± 0.05	15.1	1.5	2.4
500	14	0.31 ± 0.04	19.9	1.3	2.1
Profile 2					
40	33	0.13 ± 0.06	19	3.2	14.1
90	19	0.22 ± 0.05	13.8	1.8	7.1
150	13	0.16 ± 0.05	13	0.5	3.7
250	8	0.49 ± 0.04	12.2	0.6	2.2
500	7	0.30 ± 0.07	12	0.8	1.5
SAZ station					
40	14	0.67 ± 0.05	16.4	4.9	11.4
90	17	0.39 ± 0.05	19.8	6.6	14
150	8	0.07 ± 0.14	3.2	0.02	0.1
250	7	0.44 ± 0.06	8.6	0.7	1.8
500	12	0.52 ± 0.06	13.5	1.0	2.8
SOTS Station 2017					
Profile 1					
30	22	ND	29	10.9	43.6
70	9	ND	21	4.8	13.1
100	11	ND	20	2.7	8.2
150	13	ND	15	1.9	6.0
300	10	ND	36	2.5	4.4
500	5	ND	13	1.5	3.3
Profile 2					
70	5	ND	13	4.2	17.4
100	7	ND	11	1.8	6.8
150	16	ND	14	2.1	5.2
300	6	ND	15	2.2	3.4
500	5	ND	17	0.7	2.3
Blanks	0.58		0.11	< 0.01	0.05

because the sinking rate of particles (at 10 m day^{-1}) overwhelms the mixing (range 1.2–6 m day^{-1}) contribution to their distributions, especially during spring and summer as the mixing term reduces.

For dissolved inorganic phosphate (PO_4), the following equations express its uptake by phytoplankton to form particulate organic phosphorus (POP), its exchange between boxes and its regeneration from phytoplankton:

$$\frac{d[\mathrm{PO_4}]_{j-1}}{dt} = k_{mix} \cdot ([\mathrm{PO_4}]_j + [\mathrm{PO_4}]_{j-2}) - 2 \cdot k_{mix} \cdot [\mathrm{PO_4}]_{j-1} + k_{regen} \cdot phyto_{j-1} - \gamma_{phyto} \cdot \mu_{max.phyto} \cdot R_{N.P.phyto}[\mathrm{PO_4}]_{j-1} \quad (6)$$

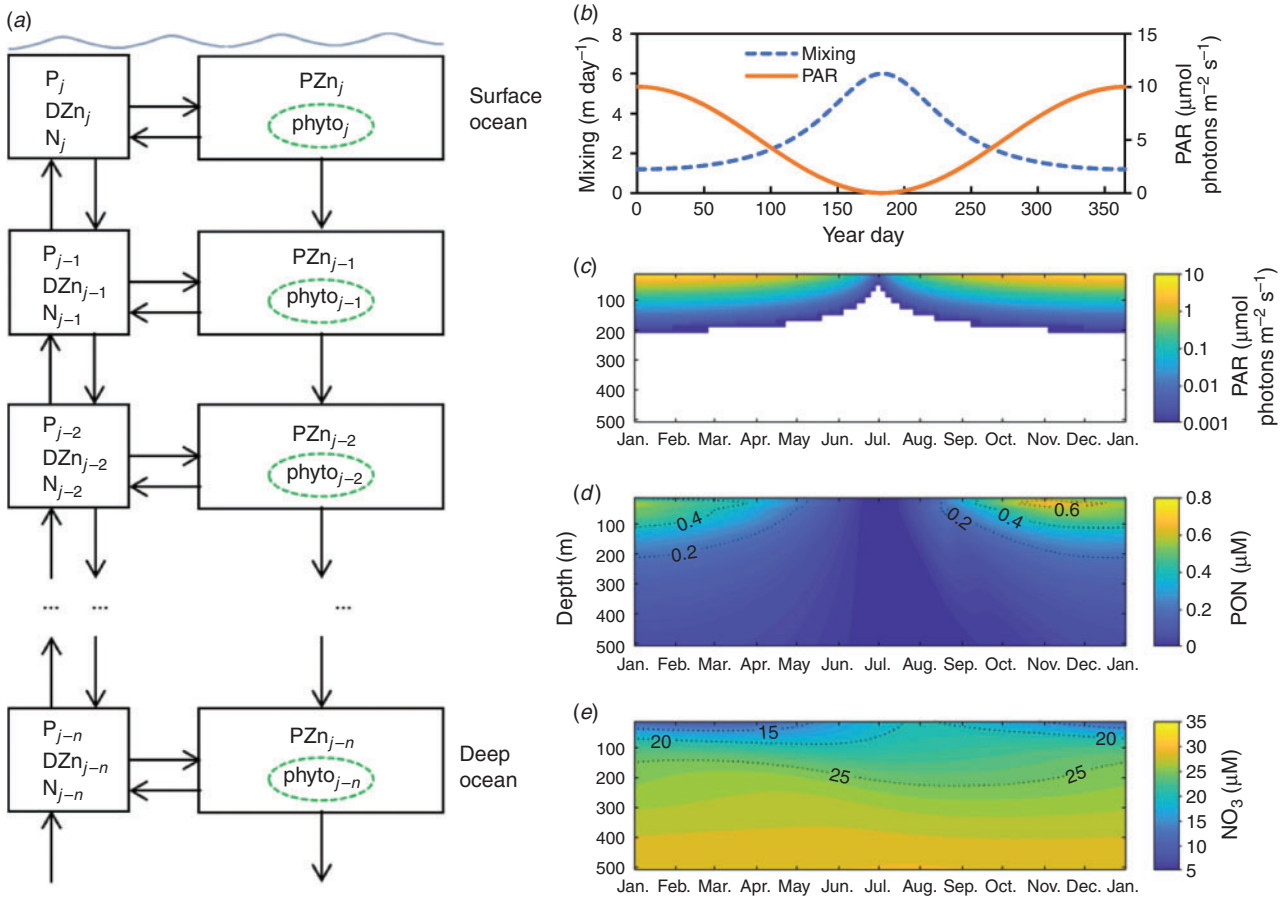

Fig. 2. (*a*) Schematic representation of the one-dimensional model configuration with dissolved nitrogen (N), phosphorous (P) and zinc (DZn), particulate Zn (PZn) and particulate N and P as phytoplankton (phyto). (*b*) Model input of seasonal variations in mixing and photosynthetically active radiation (PAR). (*c–e*) Model output of seasonal variations in depth-resolved light penetration (*c*), phytoplankton concentration expressed as particulate organic nitrogen in the model (*d*) and dissolved nitrate concentration (*e*).

$$\frac{d[\mathrm{POP}]_{j-1}}{dt} = \gamma_{phyto} \cdot \mu_{max.phyto} \cdot R_{N.P.phyto} \cdot [\mathrm{PO_4}]_{j-1} + k_{sink} \cdot [\mathrm{POP}]_j - k_{sink} \cdot [\mathrm{POP}]_{j-1} - k_{regen} \cdot [\mathrm{POP}]_j \quad (7)$$

For dZn, the following equation expresses its uptake by phytoplankton, its exchange between boxes and its regeneration from particulate matter (Zn_{phyto}):

$$\frac{d[Zn_{dissolved}]_{j-1}}{dt} = k_{mix} \cdot ([\mathrm{Zn}]_j + [\mathrm{Zn}]_{j-2}) - 2 \cdot k_{mix} \cdot [\mathrm{Zn}]_{j-1} + k_{regen} \cdot \mathrm{Zn}_{part.j-1} - \gamma_{phyto} \cdot \mu_{max.phyto} \cdot R_{N.Zn.phyto} [\mathrm{Zn^{2+}}]_{j-1} \quad (8)$$

The partitioning of zinc was between complexed and uncomplexed zinc (i.e. free inorganic zinc, Zn^{2+}) and was simulated using the following equation (Ellwood and van den Berg 2000):

$$[\mathrm{Zn^{2+}}]/[\mathrm{ZnL}] = [\mathrm{Zn^{2+}}]/C_L + 1/(C_L K'_{\mathrm{ZnL}}) \quad (9)$$

which was rearranged to give:

$$[\mathrm{Zn^{2+}}]^2 \alpha_{\mathrm{Zn}} K'_{\mathrm{ZnL}} + [\mathrm{Zn^{2+}}](\alpha_{\mathrm{Zn}} + K'_{\mathrm{ZnL}} C_L - C_{\mathrm{Zn}} K'_{\mathrm{ZnL}}) - C_{\mathrm{Zn}} = 0 \quad (10)$$

where the concentration of free zinc $[Zn^{2+}]$ in seawater was calculated as $[Zn'] = \alpha_{Zn}[Zn^{2+}]$ and C_{Zn} is the total dZn concentration, K'_{ZnL} presents the conditional stability constant for the zinc–ligand complex, C_L is the total concentration of zinc-binding ligands in solution and α_{Zn} is the coefficient for inorganic complexation of Zn^{2+} in seawater. Here K'_{ZnL}, C_L and α_{Zn} were set to 10^{10}, 1 nM and 2.1 respectively (Ellwood and van den Berg 2000; Ellwood 2004). Eqn 10 was solved within each iterative model cycle.

The overall change in particulate zinc concentration can be expressed as follows:

$$\frac{d[Zn_{particulate}]_{j-1}}{dt} = \gamma_{phyto} \cdot \mu_{max.phyto} \cdot R_{N.Zn.phyto} \cdot [Zn^{2+}]_{j-1} + k_{sink} \cdot Zn_{phyto.j} + k_{scav.Zn} \cdot [Zn^{2+}]_{j-1} - k_{sink} \cdot Zn_{part.j-1} - k_{regen.Zn} \cdot Zn_{part.j-1} \quad (11)$$

Table 3. Input parameters for the one-dimensional model used to generate profiles of dissolved zinc along with references to certain parameters used to constrain the model

CCE, Cold Core Eddy; dZn, dissolved zinc

Symbol	Description	Units	Value	Reference and notes
phyto	Phytoplankton biomass	μM (N)		
N	Dissolved inorganic nitrate (DIN)	μM		
P	Dissolved inorganic phosphate (DIP)	μM		
DZn	Dissolved inorganic zinc	nM		
POP	Particulate organic phosphorus	μM		
PZn	Particulate inorganic zinc	nM		
PAR	Photosynthetically active radiation	μmol (photons) m^{-2} s^{-1}	10	This represents the average summertime value between 0 and 20 m for the first box; PAR was adjusted to simulate a seasonal light cycle
$\mu_{max.phyto}$	Maximum overall phytoplankton growth rate	day^{-1}	0.1[A]	Adjusted to simulate the low productivity in Southern Ocean waters as a result of iron limitation (Strzepek *et al.* 2012)
$k_{phyto.N}$	Phytoplankton biomass DIN half-saturation constant	μM	0.025	Harrison *et al.* (1996), Raimbault and Garcia (2008)
$k_{phyto.P}$	Phytoplankton biomass DIP half-saturation constant	μM	0.01	Ammerman *et al.* (2003)
$k_{phyto.PAR}$	Phytoplankton biomass PAR half-saturation constant	μmol (photons) m^{-2} s^{-1}	10	
k_{mix}	Water exchange rate between boxes	m day^{-1}	1.2–6	Variable; mixing was adjusted to simulate a seasonal mixing cycle
k_{sink}	Sinking rate for particulate matter	m day^{-1}	10	
k_{regen}	Regeneration rate for particulate nitrogen, phosphorus and zinc	day^{-1}	0.35[B]	
$k_{scav.Zn}$	Scavenging rate for $[Zn^{2+}]$ from solution	day^{-1}	0 or 0.0001	For most experiments, the values were set to 0
$N_{j–n}$	DIN input flux into box *j–n*	μmol m^{-2} day^{-1}	0.048	Adjustable
$R_{N.P.phyto}$	Uptake ratio for phosphate : nitrate by phytoplankton	mol : mol	0.0625	
$R_{Zn.N.phyto}$	Uptake ratio for uncomplexed inorganic zinc : nitrate by phytoplankton	mmol : mol	32	Adjusted to mimic the dZn profile in the CCE
N.Zn.DW	Deep water N : Zn input flux supply ratio	mol : mmol	6	Adjusted to mimic the dZn profile in the CCE
N.P.DW	Deep water N : P input flux supply ratio	mol : mol	16	

[A]Phytoplankton mortality was taken from Schlosser *et al.* (2014) incorporated into cellular growth rates.
[B]This rate was held constant to the depth at which the peak biomass occurs. Below this depth the rate of regeneration decreased with depth following the Martin POC regeneration expression (Eqn 3).

For the deepest model box, box *j–n*, nitrate, phosphate and dZn were supplied into this box from below. These inputs were required to balance the loss of PON, POP and pZn associated with sinking matter that sinks out of this box.

For model runs, we simulated dissolved nitrate, phosphate and zinc profiles to a depth of 500 m with depth intervals of 20 m. Seasonality was introduced into the model by varying the light (photosynthetically activate radiation, PAR) and mixing component using a cosine function such that the light field was highest at the summer solstice (22 December) and mixing was highest during at the winter solstice (21 June), consistent with deep winter mixing during winter (Fig. 2; Tagliabue *et al.* 2014).

The model was run to an annual steady state with respect to the deeper ocean (>250 m). The model was 'calibrated' to reference profiles of nitrate and dZn from within the CCE by adjusting the supply of nutrients into the deepest box, box *j–n* (Table 3; Fig. 3).

Isotope fractionation was simulated by applying fractionation factors (α) to the following processes: Zn^{2+} uptake by phytoplankton, Zn^{2+} regeneration from organic matter, Zn^{2+} complexation by natural organic ligands and Zn^{2+} scavenging from solution. For each of these processes, the fractionation is in the expected direction for kinetic fractionation (i.e. ^{64}Zn reacts faster than ^{66}Zn), except for zinc scavenging from solution (John and Conway 2014). Thus, during uptake, phytoplankton form with isotopically lighter compositions than the dissolved Zn substrate, which, in turn, becomes progressively heavier. Regeneration preferentially releases ^{64}Zn, lightening the dZn isotope pool and rendering the remnant particle pool isotopically heavier. Understanding the effect of the ligand complexation process on dZn and pZn isotope compositions is dependent on the operational definition of 'dissolved'. As measured here, the operational separation of pZn and dZn is by filtration through a 0.2-μm pore size such that the dZn measurement is the sum of free Zn^{2+} and ligand-bound zinc. As discussed below, the ligand-bound component dominates the total dissolved pool, especially in surface waters. Thus, the Zn^{2+} released from ligands and taken up by phytoplankton is lighter than that of the operationally measured dZn, which, in turn, leads to a lighter

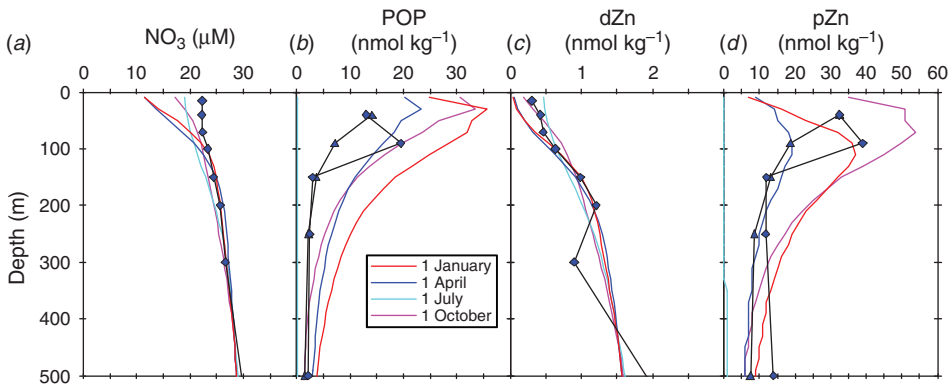

Fig. 3. Measured (Cold Core Eddy station data; blue symbols) and model profiles for 1 January, 1 April, 1 July and 1 October *v.* depth of (*a*) nitrate, (*b*) particulate organic phosphorous (POP), (*c*) dissolved zinc (dZn) and (*d*) particulate zinc (pZn).

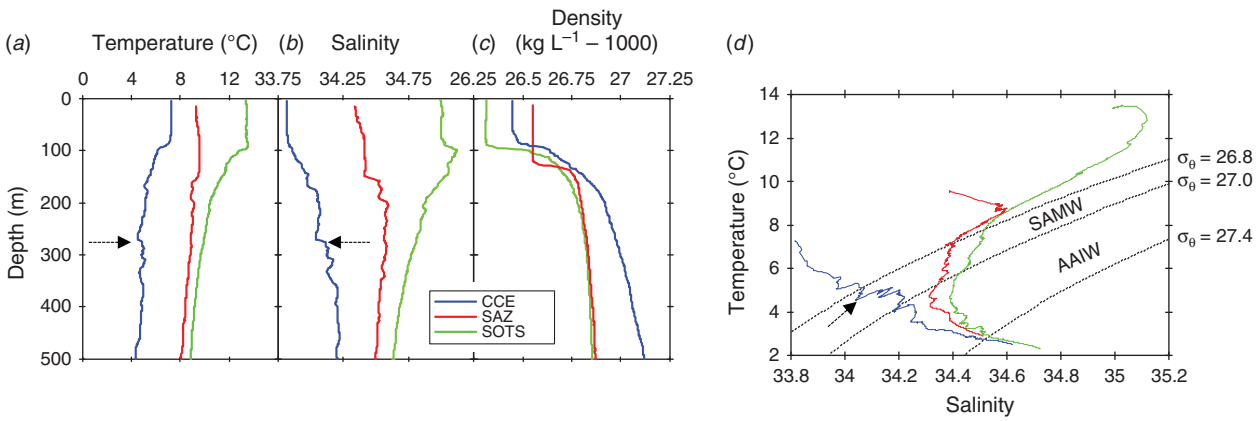

Fig. 4. Depth profiles of (*a*) temperature, (*b*) salinity and (*c*) density for the Cold Core Eddy (CCE), Subantarctic Zone (SAZ) and Southern Ocean Time Series (SOTS) stations. (*d*) Temperature *v.* salinity plot for the three stations. Constant density (σ_θ) lines are also presented for the boundaries of the Subantarctic Mode Water (SAMW) and Antarctic Intermediate Water (AAIW). Density lines were computed using the GSW Oceanographic Toolbox for Matlab (T. J. McDougall and P. M. Barker, see http://www.teos-10.org/software.htm). The arrows indicate the depth or density where the 'step' in dZn concentration occurs (see main text for details).

pZn isotope composition that would arise without the influence of ligand complexation.

Finally, special treatment is applied to the top and bottom boxes in the model. At the top, no flux enters from above. At the bottom, particles are allowed to exit the *j*–*n* box, and this is balanced by an upward supply flux of dZn and nutrients into this box. The isotope composition of the upward supply zinc is set to match the value of 0.45‰ measured for the deep Southern Ocean.

Results and discussion

Hydrography

The SOTS, CCE and SAZ stations were physically and chemically distinct (Fig. 1). The SOTS station is located along the northern edge of the SAZ close to the STF. The surface water temperature at SOTS was 12.6°C, salinity was 34.7 and nitrate and silicate concentrations were 4.5 and 1.6 μM respectively (Fig. 4), all typical of northern SAZ water properties (Rintoul and Trull 2001). The upper water column also experiences frequent incursions for subtropical water. Below the surface, SAMW and Antarctic Intermediate Water (AAIW) are present at depths of approximately 200–400 and 600–1200 m respectively (Fig. 4).

The CCE station was located at 50.4°S, 147°E within the SAZ (Fig. 1). However, the surface water temperature was 7.2°C, salinity was 33.8 (Fig. 5) and nitrate and silicate concentrations were 22 and silicate was 3.3 μM respectively, all typical of polar waters located further south of the northern extension of the SAF (Moreau *et al.* 2017; Patel *et al.* 2019). Satellite analysis revealed that the eddy had formed in early February 2016 and moved northward ~1.2° of latitude at the time of sampling (Patel *et al.* 2019). Satellite analysis of the eddy also revealed that it had a lower chlorophyll concentration than surrounding waters, consistent with its development further south in less-productive polar waters (Fig. 1, 5). Below the surface, AAIW appear to be present at depths between ~300 and 800 m within the eddy (Fig. 4).

The SAZ station was located south-east of the CCE station within the SAZ (Fig. 1). The surface water temperature for the

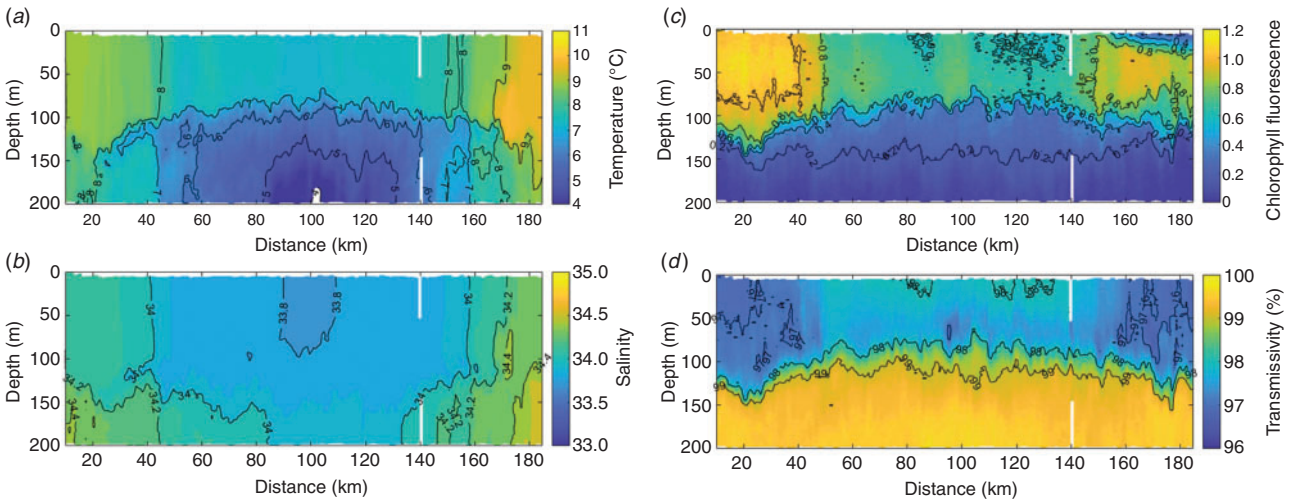

Fig. 5. TRIAXUS measurements of (*a*) temperature, (*b*) salinity, (*c*) chlorophyll fluorescence and (*d*) transmissivity across the Cold Core Eddy.

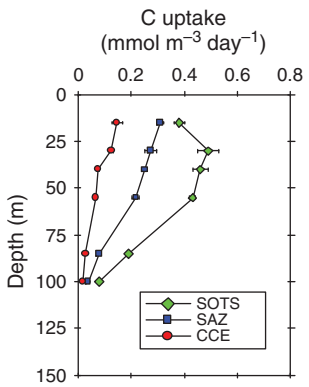

Fig. 6. Primary production rate measurements *v*. depth for the Cold Core Eddy (CCE), Subantarctic Zone (SAZ) and Southern Ocean Time Series (SOTS) stations.

SAZ station was 9.2°C, salinity was 34.3 and nitrate and silicate concentrations were 14.5 and 1.3 μM respectively (Fig. 4), again consistent with SAZ water properties (Rintoul and Trull 2001). Subsurface SAMW and AAIW were present at depths between ~200 and 1200 m (Fig. 4).

Biological and nutrient data

Aqua moderate-resolution imaging spectroradiometer (MODIS) satellite chlorophyll images reveal higher concentrations of chlorophyll at the SOTS and SAZ stations that at the CCE station (Fig. 1). Primary production rates between the three sites also varied, with the CCE station having the lowest rates, whereas the SOTS station had the highest (Fig. 6). The rates of primary production across all stations are consistent with previous measurements made for the region south of Australia (Boyd *et al.* 1999; Westwood *et al.* 2011).

The decline in the rate of primary production between stations (SOTS > SAZ > CCE) matched the decline in the dissolved iron concentration between stations within the upper water column (15–70 m) with mean (±s.d.) values of 61 ± 4, 48 ± 12 and 21 ± 3 pmol kg^{-1} for the SOTS, SAZ and CCE stations respectively (Table 1). The low rates of primary production within the CCE were matched by higher transmissivity (lower particulate mass within the water column) and lower TRIAXUS chlorophyll fluorescence than surrounding waters (Fig. 5). Our results are consistent with the prevalence of iron limitation in subantarctic and polar waters south of Australia (Boyd *et al.* 1999; Sedwick *et al.* 1999).

Upper water column concentrations for phosphate and nitrate showed varying degrees of depletion, with the SOTS station having the lowest surface water concentrations and the CCE station the highest (Fig. 7). Conversely, silicate was depleted at all three stations.

Concentrations of dZn and pZn

dZn concentrations for the three stations ranged between 0.21 and 5.06 nmol kg^{-1} across a depth range of 15–1500 m (Table 1; Fig. 7), with zinc depletion in surface waters and increasing zinc concentrations with depth. The zinc profiles, along with other dissolved profiles for iron, copper, nickel, cadmium and aluminium, were all oceanographically consistent, suggesting that contamination during sampling and analysis was minimal. For the CCE profile, there was a 'step' in the dZn concentration profile between 200 and 300 m wherein the zinc concentration decreased from 1.21 to 0.9 nmol kg^{-1}. This 'step' in zinc concentration paralleled a step-wise increase in the concentration of dissolved iron and aluminium and a slight decline in the concentration of dissolved copper, and is coincident with a change in water mass between 200 and 300 m within the CCE (Fig. 7). Analysis of temperature and salinity depth profiles for the CCE indicates that there is a change in the physical properties at ~270 m with the intrusion of water with slightly elevated temperature and salinity (Fig. 4). This 'intruding' water has a lower zinc concentration.

pZn profiles were obtained for the CCE and SAZ stations, and for at the 2017 SOTS occupation. The concentrations of pZn varied between 0.1 and 19.5 pmol kg^{-1} across a depth range of

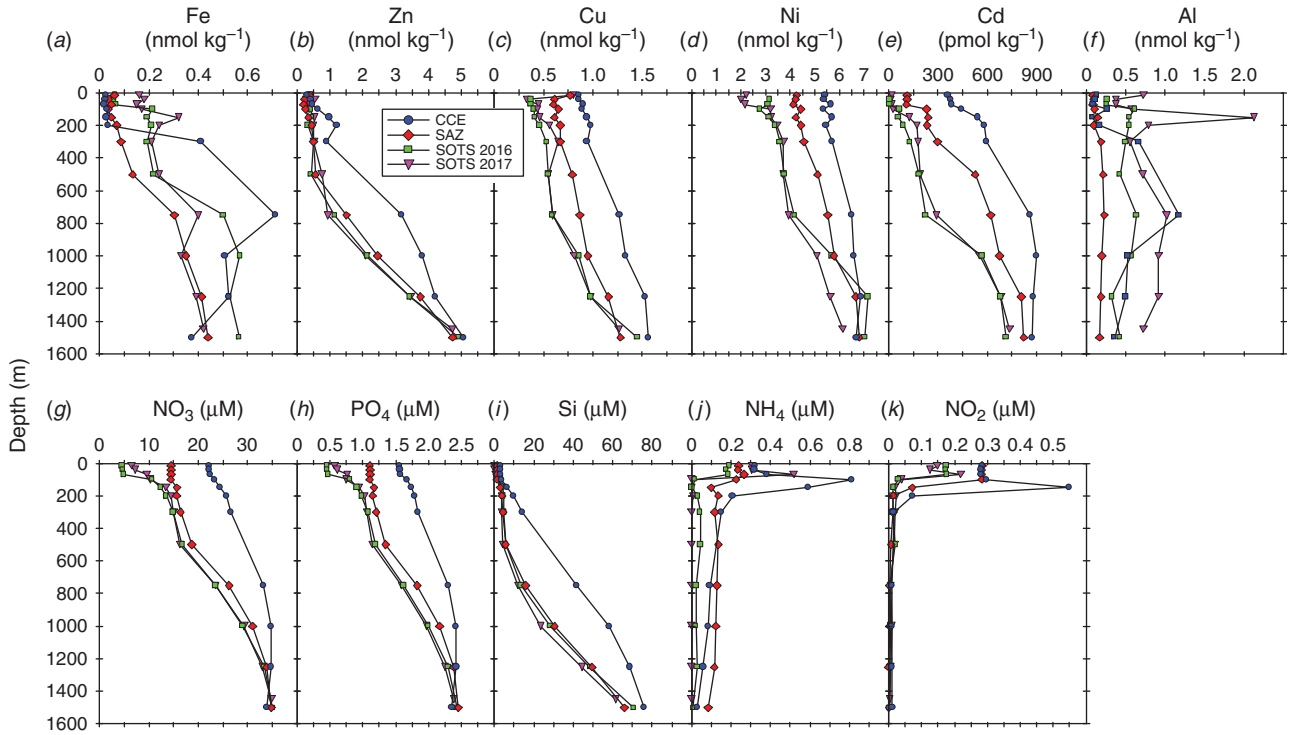

Fig. 7. Dissolved concentration *v.* depth profiles of (*a*) iron, (*b*) zinc, (*c*) copper, (*d*) nickel, (*e*) cadmium, (*f*) aluminium, (*g*) nitrate, (*h*) phosphate, (*i*) silicate, (*j*) ammonia and (*k*) nitrite for the Cold Core Eddy (CCE), Subantarctic Zone (SAZ) and Southern Ocean Time Series (SOTS) stations.

40–500 m, decreasing with depth and thus exhibiting trends opposite to the dZn profiles. The change in pZn concentration with depth is similar to that for particulate phosphorous (Fig. 8). Cadmium and copper, two metals that are also biologically used by phytoplankton, both showed enriched concentrations in the euphotic zone (Fig. 8). The particulate profiles for cadmium and copper present a nice contrast to that of zinc because dissolved cadmium is generally not expected to be scavenged from seawater, whereas dissolved copper is believed to be scavenged from seawater even though it is organically complexed. This leads to its 'hybrid' profile structure, with partial depletion in surface waters and an increase in concentration with depth (Bruland and Lohan 2003).

The attenuation of zinc with depth was modelled using the Martin equation:

$$[PZn_z] = \left[PZn_{70\,\mathrm{m}/90\,\mathrm{m}}\right]\left(\frac{z}{70\,\mathrm{m}/90\,\mathrm{m}}\right)^{-b} \qquad (12)$$

where $[PZn_z]$ represents the particulate zinc concentration at depth z, $[PZn_{70\ \mathrm{m}/90\ \mathrm{m}}]$ represents the particulate zinc concentration close to the base of the mixed layer at either 70 or 90 m and b represents the vertical attenuation factor. It should be noted that this equation was developed to model the sinking flux for particulate organic carbon and other various elements (Martin *et al.* 1987; Boyd *et al.* 2017), whereas we have used it to fit the attenuation profiles of suspended and sinking zinc, phosphorous, cadmium and copper concentration *v.* depth. That is, the suspended particle pool is dominantly produced by the attenuation of the sinking flux (Bishop 1989), with little effect of mixing. The vertical attenuation factor obtained for zinc (0.82) is less than the attenuation factors for phosphorous (2.41) and cadmium (2.41), but more than that of copper (0.28; Table 4). When normalised against phosphorous, attenuation factors for zinc, cadmium and copper are comparable to those compiled by Boyd *et al.* (2017). This sequence indicates that zinc has a longer regeneration length scale than phosphorous and cadmium, but less than that of copper (Fig. 8). That is, the regeneration of zinc is slower than that of phosphorous and cadmium but faster than that of copper. These differences in the regeneration length scale reflect the release of these metals and phosphorous from suspended and sinking cells and detrital matter. For example, zinc is used in zinc-finger proteins associated with RNA and DNA expression, carbonic anhydrase and alkaline phosphatase, all of which have different affinities for zinc (Twining *et al.* 2014). By contrast, phosphorous is a significant component of RNA and DNA, membrane phospholipids, low molecular weight water-soluble phosphate esters and metabolically active inorganic orthophosphate (Raven 2013). These differences in the regeneration of these two elements will also be reflected in the zinc : phosphorus ratio *v.* depth.

A plot of the zinc : phosphorus ratio *v.* depth revealed an increase in the ratio with increasing depth (Fig. 8). This contrasts with the results of Twining *et al.* (2014), who observed no significant change in the zinc : phosphorus ratio *v.* depth for material sinking from a diatom-dominated phytoplankton bloom from subtropical waters. Because the sampling at the SOTS, CCE and SAZ sites occurred late in the growing season, the phytoplankton community was primarily dominated by

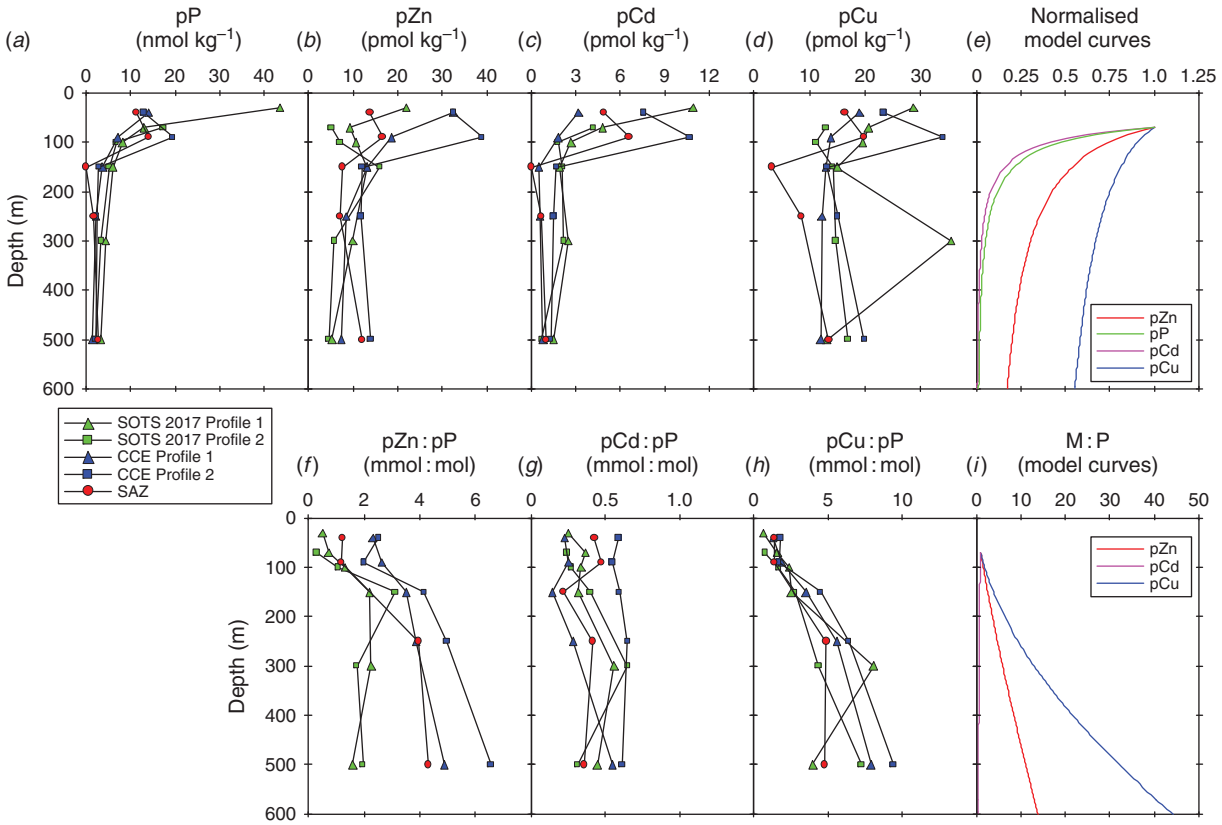

Fig. 8. Particulate concentration *v.* depth profiles of (*a*) phosphorus (pP), (*b*) zinc (pZn), (*c*) cadmium (pCd) and (*d*) copper (pCu) for the Cold Core Eddy (CCE), Subantarctic Zone (SAZ) and Southern Ocean Time Series (SOTS) stations. Note that the particulate profiles for the SOTS station were collected in 2017. (*d*) Model profile of pP, pZn, pCd and pCu normalised to concentrations at the base of the euphotic zone. Model profiles were generated using Eqn 12 with best-fit *b* factors listed in Table 4. (e–g) Particulate profiles of pZn : pP (*e*), pCd : pP (*f*) and pCu : pP (*g*) *v.* depth for the three sampling stations. (*h*) Model profiles (M) for particulate zinc, cadmium and copper ratioed to phosphorus (P).

Table 4. Vertical attenuation factors (*b* factors) for zinc, cadmium, copper and phosphorus obtained for model fits of the particulate data obtained at the Cold Core Eddy, Subantarctic Zone and Southern Ocean Time Series stations

Model fits of the particulate data were undertaking using a least-squares fitting routine to the Martin power law equation for the vertical attenuation of each particle element concentration *v.* depth. ND, no data. Values for Boyd *et al.* (2017) data are ±1 s.d.

	Zn	Cd	Cu	P
Present study	0.82	2.41	0.28	2.04
Scaled to P	0.40	1.18	0.14	1.00
Boyd *et al.* (2017)	0.77 ± 0.34	ND	0.09 ± 0.38	0.88 ± 0.48
Boyd *et al.* (2017) scaled to P	0.88	ND	0.10	1.00

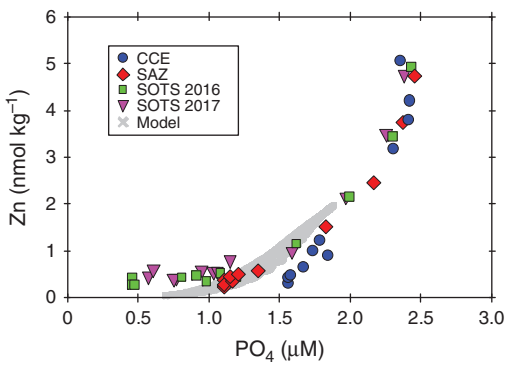

Fig. 9. Dissolved zinc *v.* phosphate for samples collected at the Cold Core Eddy (CCE), Subantarctic Zone (SAZ) and Southern Ocean Time Series (SOTS) stations and seasonal model runs.

small prokaryote and eukaryote phytoplankton, which may explain the difference between these two studies.

The differential regeneration of zinc relative to phosphorus should also be reflected in the dissolved phase for these two elements, whereby it is expected that the increase in dZn concentration with depth should be lower than that of phosphate. A plot of zinc *v.* phosphate shows curvature where the slope for the relative change in the dZn and phosphate concentration (ΔZn/ΔP) increases with depth (Fig. 9), which can be interpreted as faster phosphorus regeneration relative to zinc.

Recent ocean modelling work of the biogeochemical zinc cycle used a range of approaches to simulate its cycling. In general, the uptake and regeneration of zinc in these models is tied to that of phosphorus (Vance *et al.* 2017; de Souza *et al.*

2018; Roshan *et al.* 2018; Weber *et al.* 2018). Our modelling results also show that there is a decoupling between zinc and phosphate (and nitrate) cycling resulting from differences in the stoichiometric Zn : P uptake ratio relative to the deep-water Zn : P supply ratio (Fig. 9; Sunda and Huntsman 1992). This decoupling is likely to be amplified by differences in the regeneration length scale between these two elements: in most models, the regeneration rate of these two elements is assumed to be similar (e.g. Vance *et al.* 2017). Our field results suggest that this is not quite the case; rather, we find that zinc is less labile than phosphorous, leading to a longer regeneration length scale. These differences in regeneration length scales may seem small, but they strongly affect the biogeochemical coupling, or the lack thereof, for these two elements.

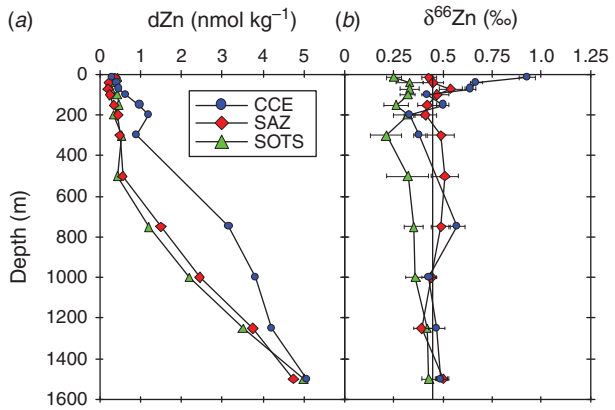

Fig. 10. Profiles of (*a*) dissolved zinc (dZn) concentration and (*b*) dissolved zinc isotope composition ($\delta^{66}Zn$) *v.* depth for the Cold Core Eddy (CCE), Subantarctic Zone (SAZ) and Southern Ocean Time Series (SOTS) stations. The solid vertical line in (*b*) was set to 0.45‰ and represents the value that best describes the $\delta^{66}Zn_{dissolved}$ of the deep Southern Ocean. Error bars represent 2 s.e.m. for isotope measurements.

Zinc isotope analysis

The isotope composition of dZn ($\delta^{66}Zn_{dissolved}$) varied between 0.21 and 0.93‰, with most of the variability occurring in the upper water column at the CCE station, where values ranged from 0.93 to 0.33‰ between depths of 40 and 200 m (Fig. 10, 11). For the other two stations, $\delta^{66}Zn_{dissolved}$ showed less variability, with values ranging between 0.32 and 0.54‰ at depths between 40 and 200 m. Mean (±2s.d.) deep-water (≥1000 m) values for $\delta^{66}Zn_{dissolved}$ were 0.46 ± 0.06, 0.44 ± 0.11 and 0.40 ± 0.08‰ for the CCE, SAZ and SOTS stations respectively. These deep-water values are consistent with other Southern Ocean deep-water (≥700 m) measurements (e.g. Wang *et al.* 2018), where mean (±2s.d.) $\delta^{66}Zn_{dissolved}$ was 0.40 ± 0.05‰ (n = 13).

The $\delta^{66}Zn_{dissolved}$ values measured at the SOTS station between 300 and 1000 m were isotopically lighter than measurements made across the same depth range at the other two stations (Fig. 10). That said, these lower $\delta^{66}Zn_{dissolved}$ values at the SOTS station were consistent with measurements made by Samanta *et al.* (2017) across a similar depth range for a station located east (Station P3; located at 46.2°S, 159.5°E) of the SOTS site, but at a similar latitude. This light $\delta^{66}Zn_{dissolved}$ signal at the SOTS station may represent the influence the Tasman Sea Outflow (Oliver and Holbrook 2014), which forms part of the South Pacific super gyre (Ridgway 2007).

The isotope composition of particulate zinc ($\delta^{66}Zn_{particulate}$) varied between 0.07 and 0.67‰ (Fig. 11). For the CCE station, $\delta^{66}Zn_{particulate}$ values were lighter in the upper water column and increased to values ~0.44‰ at a depth of 250 m. These lighter $\delta^{66}Zn_{particulate}$ values occur within the euphotic zone (40 m) when $\delta^{66}Zn_{dissolved}$ is isotopically heavy, suggesting that uptake of isotopically light zinc by cells (John *et al.* 2007; Samanta *et al.* 2017) resulted in the dZn pool becoming isotopically heavy (Fig. 11).

By contrast, $\delta^{66}Zn_{particulate}$ values for the SAZ site profile varied between 0.07 and 0.67‰, with the minimum occurring at 150 m below the euphotic zone (Fig. 11). This minimum occurs at the transition from higher to lower nitrate and ammonia

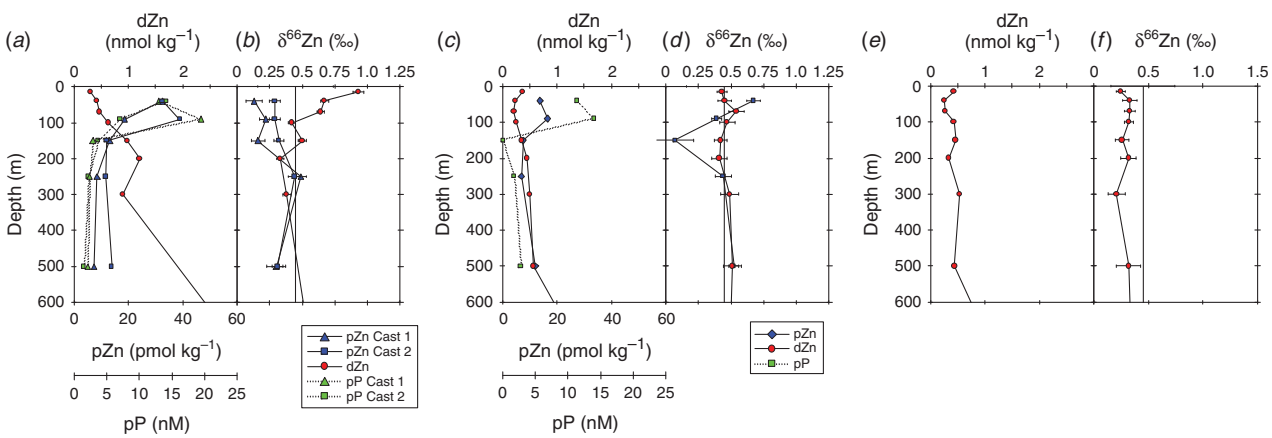

Fig. 11. (*a*) Upper ocean (0–500 m) profiles of dissolved zinc (dZn), particulate zinc (pZn) and particulate phosphorus (pP) concentrations *v.* depth for the Cold Core Eddy (CCE) station. (*b*) Isotope composition of dZn and pZn *v.* depth for the CCE station. (*c*) Profiles of dZn, pZn and pP concentrations *v.* depth for the Subantarctic Zone (SAZ) station. (*d*) Isotope composition of dZn and pZn *v.* depth for the SAZ station. (*e*) Profile of dZn *v.* depth for the Southern Ocean Time Series (SOTS) station. (*f*) Isotope composition of dZn *v.* depth for the SOTS station.

concentrations, which is indicative of particulate organic matter regeneration (Fig. 7). Below 150 m, mean (±2s.d.) $\delta^{66}Zn_{particulate}$ increases to values near the deep-water average of 0.44 ± 0.11‰ for the SAZ site. Note that we did not collect particulate samples during the 2016 SOTS site occupation, so we do not have $\delta^{66}Zn_{particulate}$ values to compare with the $\delta^{66}Zn_{dissolved}$ profile obtained at this site.

Upper ocean $\delta^{66}Zn_{dissolved}$ fractionation

Observations

The upper water column values (0–100 m) within the CCE and at the SAZ station revealed an increase in $\delta^{66}Zn_{dissolved}$ values with increasing dZn concentration. The $\delta^{66}Zn_{dissolved}$ distribution is consistent with preferential loss of ^{64}Zn through uptake by phytoplankton accompanying the observed surface deficit of dZn concentrations. To explore this further, we plotted $\delta^{66}Zn_{dissolved}$ against ln[Zn] for the CCE because it is essentially a closed system with regard to the surrounding waters, thus allowing us to use a closed-system Rayleigh fractionation model to model the data (Fig. 12). Fitting the model to the $\delta^{66}Zn_{dissolved}$ data produced a mean (±s.d.) fractionation factor (α) of 0.999 33 ± 0.000 04 ($\varepsilon = -0.67$‰) for samples collected within the euphotic zone (0–100 m). Interestingly, the $\delta^{66}Zn_{particulate}$ data did not conform to either the instantaneous or expected integrated fractionation process associated with the closed-system model (Fig. 12). The expectation is that as dZn is depleted and $\delta^{66}Zn_{dissolved}$ increases towards the surface, $\delta^{66}Zn_{particulate}$ will also increase for both the instantaneous product (for which $\delta^{66}Zn_{particulate}$ should track $\delta^{66}Zn_{dissolved}$ with a constant offset of −0.67) and for the accumulated product (Fig. 12). Instead, $\delta^{66}Zn_{particulate}$ varies little with changes in dZn concentration.

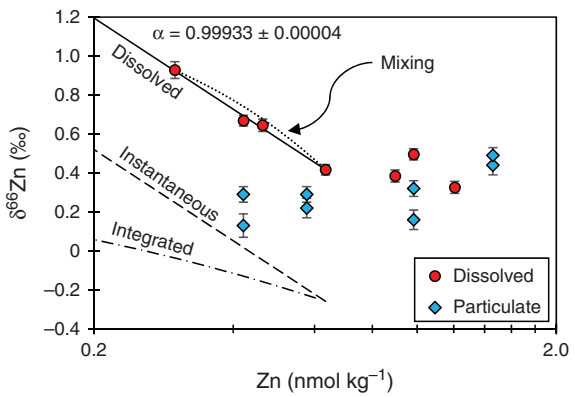

Fig. 12. Plot of the isotope composition for dissolved and particulate zinc plotted against dissolved zinc concentrations depth for the Cold Core Eddy. The dissolved zinc isotope fractionation factor (α) was obtained by fitting the following equation: $\delta^{66}Zn_{dissolved} = \delta^{66}Zn_{100\ m} - \varepsilon\ln(f)$, where ε is the isotope fractionation factor between the product (biologically used zinc) and the substrate (dissolved zinc) and f is dissolved zinc between 15 and 100 m divided by the dissolved zinc concentration at 100 m. The instantaneous production model curve was produced using the equation $\delta^{66}Zn_{particulate} = \delta^{66}Zn_{dissolved} + \varepsilon$, whereas the integrated model curve was produced using the equation $\delta^{66}Zn_{particulate} = \delta^{66}Zn_{100\ m} - \varepsilon\ln(f \cdot \ln(f) \div (1-f))$. A binary mixing line is also shown for samples collected within the upper 100 m.

The primary production profiles offer a possible explanation for this discrepancy: because pZn is generated primarily in the euphotic zone at depths less than 50 m where primary production is highest (Fig. 6), the difference in the $\delta^{66}Zn_{particulate}$ and $\delta^{66}Zn_{dissolved}$ distributions is driven by the different mechanisms of their vertical redistribution. Hence, the $\delta^{66}Zn_{particulate}$ signature is distributed downward without modification by sinking, whereas changes in the $\delta^{66}Zn_{dissolved}$ with depth (or dZn concentration) across the euphotic likely represents a mixing curve.

Below the depth of maximum biomass (i.e. below ~100 m), the $\delta^{66}Zn_{particulate}$ signature increases subtly (Fig. 11). One interpretation is that this occurs as a result of remineralisation, which preferentially releases ^{64}Zn so the remaining pZn pool becomes heavier and, correspondingly, the $\delta^{66}Zn_{dissolved}$ pool becomes lighter where they converge near 250m (Fig. 12). We tested this idea with our 1-D model.

1-D modelling

The changes in $\delta^{66}Zn_{dissolved}$ between 0 and 100 m, resulting in the apparent ε of −0.67‰, could be a consequence of several processes including: (1) complexation to natural organic ligands; (2) biological fractionation within the euphotic zone; and (3) isotope fractionation upon zinc regeneration from organic matter. Here we explore these processes further in the 1-D model by running it over a yearly cycle to mimic the seasonal conversion of dZn to pZn within the euphotic zone followed by the remineralisation of pZn at depth. Data were then extracted data close to the time of sampling of the CCE.

It has been argued that the fractionation of zinc isotopes in phytoplankton culture studies results from its partitioning between inorganic and organic complexes (e.g. by EDTA, which is used to buffer the inorganic zinc concentration of the medium; John *et al.* 2007). Zinc-EDTA isotope fractionation is ~0.3‰ between complexed and Zn^{2+} with the zinc-EDTA being isotopically heavy (Ban *et al.* 2002; Ding *et al.* 2010; Marković *et al.* 2017). In seawater, zinc speciation is dominated by its complexation with natural organic ligands (Bruland 1989; Ellwood and van den Berg 2000; Ellwood 2004) with ligand concentrations ranging between 1 and 2 nM. Using a natural ligand concentration for the subantarctic waters of 1 nM with a conditional stability constant of 10^{10} (Ellwood 2004), we found that complexation results in $\delta^{66}Zn_{dissolved}$ (which reflects the sum of the ligand-bound and free Zn^{2+} components) becoming isotopically heavy in surface waters when using a value of $\varepsilon_{complexation} = 0.3$‰ ($\delta^{66}Zn_{Zn2+} - \delta^{66}Zn_{dissolved}$; $\alpha_{complexation} = 1.0003$). However, the extent of the change in both $\delta^{66}Zn_{dissolved}$ and $\delta^{66}Zn_{particulate}$ did not match our observations particularly well for the time of sampling of the CCE (Fig. 13).

Zinc isotope fractionation can also occur during Zn^{2+} uptake by phytoplankton (John *et al.* 2007; Köbberich and Vance 2017; Samanta *et al.* 2018). Using fractionation factors of $\varepsilon_{uptake} = -0.3$‰ ($\delta^{66}Zn_{dissolved} - \delta^{66}Zn_{particulate}$; $\alpha_{uptake} = 0.9997$) or −0.67‰ (Fig. 12) for zinc uptake by phytoplankton, $\delta^{66}Zn_{dissolved}$ becomes isotopically heavy in surface waters of the model. However, the extent of change in both $\delta^{66}Zn_{dissolved}$ and $\delta^{66}Zn_{particulate}$ did not match our observations well; rather, the model simulation was isotopically heavy compared with the field data (Fig. 13).

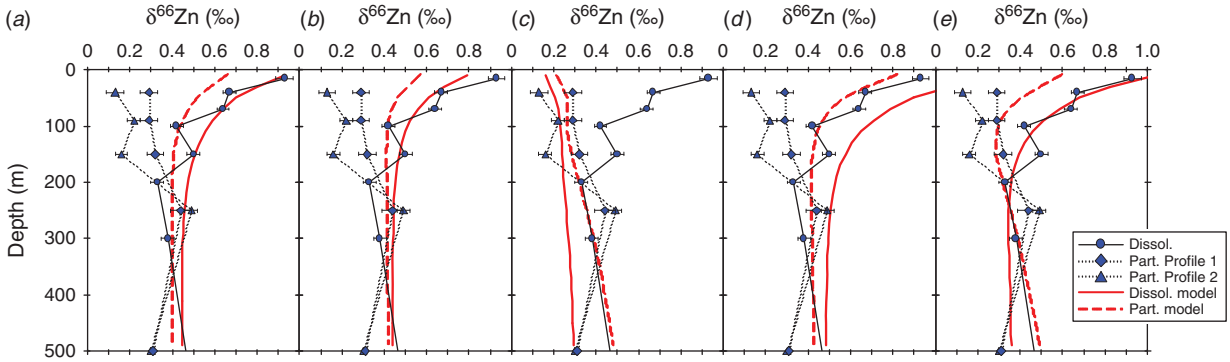

Fig. 13. (*a*) Modelled (red lines) and measured (blue symbols) profiles of the isotope composition of dissolved (Dissol.) and particulate (Part.) zinc *v.* depth for the core eddy station; $\varepsilon_{uptake} = -0.3‰$, $\varepsilon_{complexation} = 0‰$ and $\varepsilon_{regeneration} = 0‰$. (*b*) Same as in (*a*), but $\varepsilon_{uptake} = 0‰$, $\varepsilon_{complexation} = 0.3‰$ and $\varepsilon_{regeneration} = 0‰$. (*c*) Same as in (*a*), but $\varepsilon_{uptake} = 0‰$, $\varepsilon_{complexation} = 0‰$ and $\varepsilon_{regeneration} = 0.15‰$. (*d*) Same as in (*a*), but $\varepsilon_{uptake} = -0.3‰$, $\varepsilon_{complexation} = 0.3‰$ and $\varepsilon_{regeneration} = 0‰$. (*e*) Same as in (*a*), but $\varepsilon_{uptake} = -0.3‰$, $\varepsilon_{complexation} = 0.3‰$ and $\varepsilon_{regeneration} = 0.15‰$.

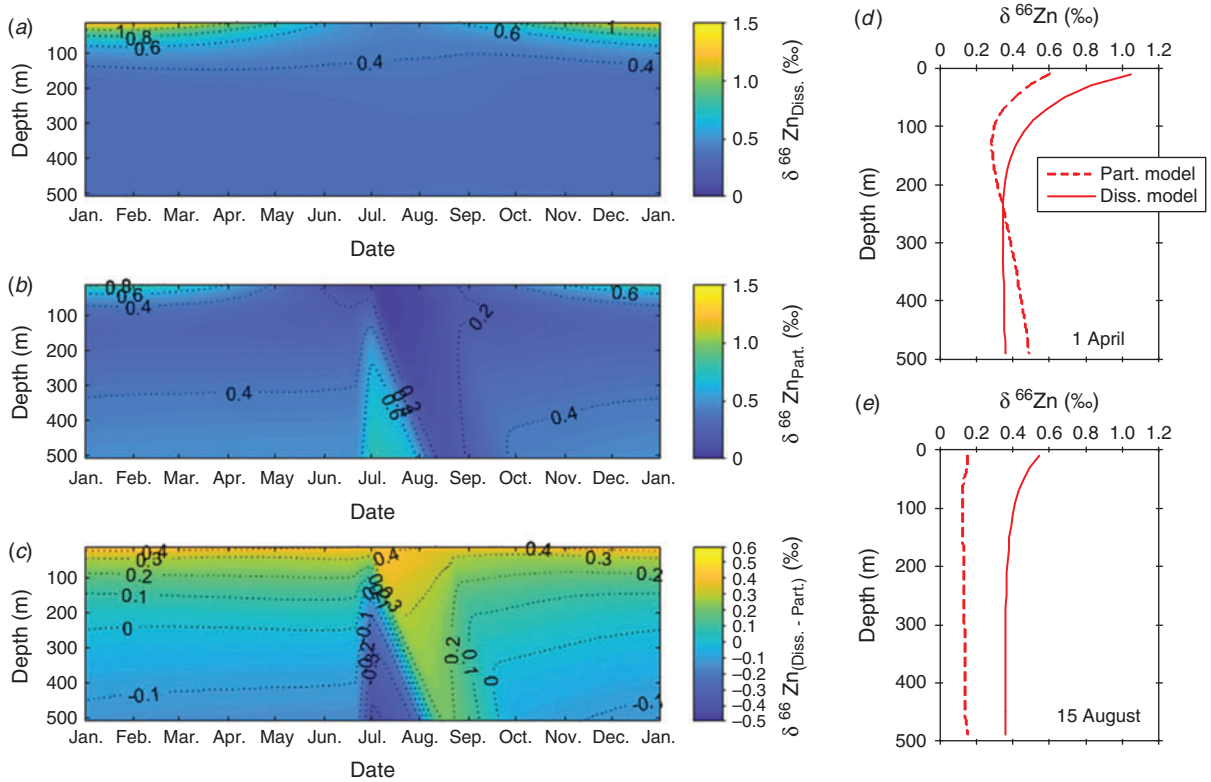

Fig. 14. Upper ocean (0–500 m) seasonal sections of the isotope composition of (*a*) dissolved zinc ($\delta^{66}Zn_{Diss.}$), (*b*) particulate zinc ($\delta^{66}Zn_{Part.}$) and (*c*) $\Delta^{66}Zn_{(Diss. - Part.)}$. For these experiments $\varepsilon_{uptake} = -0.3‰$, $\varepsilon_{complexation} = 0.3‰$ and $\varepsilon_{regeneration} = 0.15‰$. (*d*, *e*) Model depth profiles of $\delta^{66}Zn_{dissolved}$ and $\delta^{66}Zn_{partcilate}$ for 1 April (*d*) and 15 August (*e*).

We simulated the effect of fractionation associated with both zinc complexation with natural organic ligands and Zn^{2+} uptake by phytoplankton using $\varepsilon_{complexation}$ set to 0.3‰ and $\varepsilon_{uptake} = -0.3‰$. The combined influence of these process produced a $\delta^{66}Zn_{dissolved}$ that was similar in structure to the measured values for the CCE station (Fig. 13). However, the modelled $\delta^{66}Zn_{particulate}$ did not fit the measured data particularly well for the time of sampling of the CCE. Indeed, the measured data are subtly lighter within and below the euphotic zone, whereas the modelled data remain close to the deep-water input value.

Experimentation with the 1-D model revealed that including fractionation of zinc upon its regeneration from particulate organic matter improved the best fit to the CCE dataset. Setting

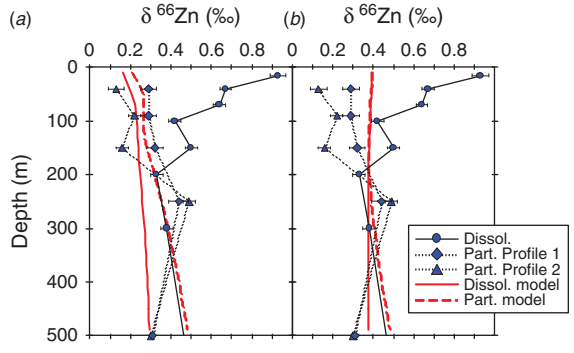

Fig. 15. (*a*) Modelled (red lines) and measured (blue symbols) profiles of the isotope composition of dissolved (Dissol.) and particulate (Part.) zinc *v.* depth for the core eddy station; $\varepsilon_{regeneration} = -0.15‰$. (*b*) Same as in (*a*), but $\varepsilon_{regeneration} = 0.58‰$ (John and Conway 2014).

a value for $\varepsilon_{regeneration}$ to −0.15‰ ($\delta^{66}Zn_{particulate} - \delta^{66}Zn_{dissolved}$; $\alpha_{complexation} = 0.99985$) in combination with $\varepsilon_{complexation}$ and ε_{uptake} values of 0.3 and −0.3‰ respectively produced the best fit to the measured values for both $\delta^{66}Zn_{dissolved}$ and $\delta^{66}Zn_{particulate}$ datasets (Fig. 13). That is, it appears that the combined effect of zinc isotope fractionation occurs as a result of complexation with natural organic ligands, zinc uptake and zinc regeneration from sinking particulate organic matter. These 1-D model results also confirm that sinking can redistribute the $\delta^{66}Zn_{particulate}$ signature so that it is homogeneous above 150 m. It also confirms that remineralisation can cause the $\delta^{66}Zn_{dissolved}$ and $\delta^{66}Zn_{particulate}$ signatures to converge at depths between 150 and 250 m (Fig. 14*d*).

Using a 1-D model, John and Conway (2014) were able to demonstrate that the scavenging ($\alpha_{scavenging}$ ranging between 1.00058 and 1.001) of zinc from solution onto particles can lead to a light $\delta^{66}Zn_{dissolved}$ composition and heavy $\delta^{66}Zn_{particulate}$ composition. This is akin to what we model for zinc being regenerated for sinking particulate matter (Fig. 15). We found the role of scavenging is weak in the upper portion of the profile as a result of zinc complexation with natural organic ligands, which reduces the concentration dissolved free zinc available to be scavenged. Note that the model of John and Conway (2014) did not include organic complexation of zinc, so its effect in their model was not tested. As our results show (Fig. 15), a combination of processes can reproduce the structure seen for the in-eddy $\delta^{66}Zn_{dissolved}$ and $\delta^{66}Zn_{particulate}$ profiles, without the specific requirement for scavenging. Indeed, zinc isotope fractionation during organic matter regeneration needs to be considered in global-scale models along with differential zinc regeneration relative to the release of nutrients from sinking particles.

The nutrient and zinc concentrations and isotope distributions should be considered as reflecting autumn conditions for phytoplankton production, export and remineralisation. Our 1-D model runs show that phytoplankton production, export and remineralisation vary seasonally and that the isotope signatures of dZn and pZn zinc are dynamic (Fig. 14). Interestingly, the period when $\delta^{66}Zn_{dissolved}$ and $\delta^{66}Zn_{particulate}$ signatures do diverge and show Rayleigh-like fractionation characteristics is during the initial phytoplankton development between August and September (Fig. 14). This occurs as a result of strong winter mixing, which resets water column biogeochemistry to near deep-water values and low particulate production during winter months as a result of light limitation. These two factors, combined with the remineralisation and vertical redistribution of the low number of particles present during winter, allow the system to be reset to conditions comparable to a 'classic' closed system.

Overall, our work shows that the $\delta^{66}Zn$ signature for both the dZn and pZn phases is affected by chemical (complexation), biological (uptake and regeneration) and physical (mixing and particle sinking) processes that, combined, influence the dissolved and particulate isotopic fields. Zinc scavenging onto particles appears to play a minor role in setting the $\delta^{66}Zn$ signature for both dZn and pZn when zinc-complexing ligands are undersaturated. It is only through the use of a model, which included seasonality, that we could evaluate the relative importance of these processes.

Conclusions

Profiles of dZn concentration *v.* depth collected at three stations located in the SAZ showed depletion in surface waters and enrichment at depth. By contrast, profiles of pZn concentration *v.* depth profiles showed enrichment within the euphotic zone, followed by a decline in concentration with depth. The structure of the pZn concentration profile was similar to that of particulate phosphorus and cadmium, but contrasted that of copper. Modelling of these particulate profiles produced variable vertical attenuation factors of 0.82, 2.04, 2.41 and 0.28 for zinc, phosphorus, cadmium and copper respectively. Our results indicate that zinc has a longer regeneration length scale than phosphorus and cadmium, but a shorter one than copper. These differences likely help explain differences in the structures of the dissolved concentration *v.* depth profiles for these elements.

Profiles of $\delta^{66}Zn_{dissolved}$ *v.* depth showed enrichment (mean ± 2 s.e., 0.93 ± 0.04‰) in surface waters relative to deep (>1000 m) waters (0.46 ± 0.06‰) for the CCE station. Because of its isolated nature, the $\delta^{66}Zn_{dissolved}$ from the CCE station likely retains the signals of isotope fractionation, whereas at the SOTS and SAZ stations these may have been lost or diluted through physical processes such as mixing. Using a 1-D model, we showed that the isotopic structure of the $\delta^{66}Zn_{dissolved}$ and $\delta^{66}Zn_{particulate}$ profiles from the CCE station can be explained by the combined effects of isotope fractionation associated with uptake by phytoplankton, complexation of zinc with natural organic ligands and the regeneration of zinc from particulate matter. It appears that the role of scavenging is minor in the upper ocean where zinc complexation dominates.

Conflicts of interest

M. J. Ellwood is a Guest Editor of the research front dedicated to Prof. Keith Hunter. Despite this relationship, he did not at any stage have editorial-level access to the manuscript while it was in peer review. *Marine and Freshwater Research* encourages its editors to publish in the journal and they are kept totally separate from the decision-making processes for their manuscripts. The authors have no further conflicts of interest to declare.

Declaration of funding

This research was supported financially under the Australian Research Council's Discovery Program (DP170102108; DP130100679) and ship time from Australia's Marine National Facility (IN2016_V02 and IN2017_V02).

Acknowledgements

This paper is dedicated to Prof. Keith Hunter, who passed away on 24 October 2018. To the senior authors of this paper, Keith was an inspiration. Keith was a true academic with an in-depth knowledge of all things marine and anything else he turned his attention too. As a testament, many of the figures generated in this paper were undertaken using a spreadsheet program (ViewFinder) written by Keith. Keith was also a great leader and mentor, and his wise counsel will be missed by the senior authors of this paper. The authors are grateful to the officers, crew and research staff of the Marine National Facility *RV Investigator* for their help with sample collection and generation of hydrochemistry data.

References

Ammerman, J. W., Hood, R. R., Case, D. A., and Cotner, J. B. (2003). Phosphorus deficiency in the Atlantic: an emerging paradigm in oceanography. *Eos* **84**(18), 165–170. doi:10.1029/2003EO180001

Archer, C., Andersen, M. B., Cloquet, C., Conway, T. M., Dong, S., Ellwood, M., Moore, R., Nelson, J., Rehkamper, M., Rouxel, O., Samanta, M., Shin, K.-C., Sohrin, Y., Takano, S., and Wasylenki, L. (2017). Inter-calibration of a proposed new primary reference standard AA-ETH Zn for zinc isotopic analysis. *Journal of Analytical Atomic Spectrometry* **32**(2), 415–419. doi:10.1039/C6JA00282J

Armstrong, F. A. J., Stearns, C. R., and Strickland, J. D. H. (1967). The measurement of upwelling and subsequent biological process by means of the Technicon Autoanalyzer and associated equipment. *Deep-Sea Research and Oceanographic Abstracts* **14**(3), 381–389. doi:10.1016/0011-7471(67)90082-4

Ban, Y., Aida, M., Nomura, M., and Fujii, Y. (2002). Zinc isotope separation by ligand exchange chromatography using cation exchange resin. *Journal of Ion Exchange* **13**(2), 46–52. doi:10.5182/JAIE.13.46

Bishop, J. K. B. (1989). Regional extremes in particulate matter composition and flux: effects on the chemistry of the ocean interior. In 'Productivity of the Ocean: Present and Past'. (Eds W. H. Berger, V. S. Smetacek, and G. Wefer.) pp. 117–137. (Wiley: New York, NY, USA.)

Boyd, P., LaRoche, J., Gall, M., Frew, R., and McKay, R. M. L. (1999). Role of iron, light, and silicate in controlling algal biomass in subantarctic waters SE of New Zealand. *Journal of Geophysical Research – Oceans* **104**, 13395–13408. doi:10.1029/1999JC900009

Boyd, P. W., Law, C. S., Hutchins, D. A., Abraham, E. R., Croot, P. L., Ellwood, M., Frew, R. D., Hadfield, M., Hall, J., Handy, S., Hare, C., Higgins, J., Hill, P., Hunter, K. A., LeBlanc, K., Maldonado, M. T., McKay, R. M., Mioni, C., Oliver, M., Pickmere, S., Pinkerton, M., Safi, K., Sander, S., Sanudo-Wilhelmy, S. A., Smith, M., Strzepek, R., Tovar-Sanchez, A., and Wilhelm, S. W. (2005). FeCycle: attempting an iron biogeochemical budget from a mesoscale SF_6 tracer experiment in unperturbed low iron waters. *Global Biogeochemical Cycles* **19**(4), GB4S2. doi:10.1029/2005GB002494

Boyd, P. W., Ellwood, M. J., Tagliabue, A., and Twining, B. S. (2017). Biotic and abiotic retention, recycling and remineralization of metals in the ocean. *Nature Geoscience* **10**(3), 167–173. doi:10.1038/NGEO2876

Bruland, K. W. (1989). Complexation of zinc by natural organic ligands in the Central North Pacific. *Limnology and Oceanography* **34**(2), 269–285. doi:10.4319/LO.1989.34.2.0269

Bruland, K. W., and Lohan, M. C. (2003). 6.02 – Controls of trace metals in seawater A2 – Holland, Heinrich D. In 'Treatise on Geochemistry'. (Ed. K. K. Turekian.) pp. 23–47. (Pergamon: Oxford, UK.)

Bruland, K. W., Knauer, G. A., and Martin, J. H. (1978). Zinc in north-east Pacific water. *Nature* **271**(5647), 741–743. doi:10.1038/271741A0

Butler, E. C. V., O'Sullivan, J. E., Watson, R. J., Bowie, A. R., Remenyi, T. A., and Lannuzel, D. (2013). Trace metals Cd, Co, Cu, Ni, and Zn in waters of the subantarctic and Polar Frontal Zones south of Tasmania during the 'SAZ-Sense' project. *Marine Chemistry* **148**, 63–76. doi:10.1016/J.MARCHEM.2012.10.005

Cloquet, C., Carignan, J., Lehmann, M., and Vanhaecke, F. (2008). Variation in the isotopic composition of zinc in the natural environment and the use of zinc isotopes in biogeosciences: a review. *Analytical and Bioanalytical Chemistry* **390**(2), 451–463. doi:10.1007/S00216-007-1635-Y

de Souza, G. F., Khatiwala, S. P., Hain, M. P., Little, S. H., and Vance, D. (2018). On the origin of the marine zinc–silicon correlation. *Earth and Planetary Science Letters* **492**, 22–34. doi:10.1016/J.EPSL.2018.03.050

Ding, X., Nomura, M., and Fujii, Y. (2010). Zinc isotope effects by chromatographic chelating exchange resin. *Progress in Nuclear Energy* **52**(2), 164–167. doi:10.1016/J.PNUCENE.2009.06.003

Eggimann, D. W., and Betzer, P. R. (1976). Decomposition and analysis of refractory oceanic suspended materials. *Analytical Chemistry* **48**(6), 886–890. doi:10.1021/AC60370A005

Ellwood, M. J. (2004). Zinc and cadmium speciation in subantarctic waters east of New Zealand. *Marine Chemistry* **87**(1–2), 37–58. doi:10.1016/J.MARCHEM.2004.01.005

Ellwood, M. J. (2008). Wintertime trace metal (Zn, Cu, Ni, Cd, Pb and Co) and nutrient distributions in the Subantarctic Zone between 40–52°S; 155–160°E. *Marine Chemistry* **112**, 107–117. doi:10.1016/J.MARCHEM.2008.07.008

Ellwood, M. J., and van den Berg, C. M. G. (2000). Zinc speciation in the northeastern Atlantic Ocean. *Marine Chemistry* **68**(4), 295–306. doi:10.1016/S0304-4203(99)00085-7

Ellwood, M. J., Hutchins, D. A., Lohan, M. C., Milne, A., Nasemann, P., Nodder, S. D., Sander, S. G., Strzepek, R., Wilhelm, S. W., and Boyd, P. W. (2015). Iron stable isotopes track pelagic iron cycling during a subtropical phytoplankton bloom. *Proceedings of the National Academy of Sciences of the United States of America* **112**(1), E15–E20. doi:10.1073/PNAS.1421576112

Franck, V. M., Smith, G. J., Bruland, K. W., and Brzezinski, M. A. (2005). Comparison of size-dependent carbon, nitrate, and silicic acid uptake rates in high- and low-iron waters. *Limnology and Oceanography* **50**(3), 825–838. doi:10.4319/LO.2005.50.3.0825

Frölicher, T. L., Sarmiento, J. L., Paynter, D. J., Dunne, J. P., Krasting, J. P., and Winton, M. (2015). Dominance of the Southern Ocean in anthropogenic carbon and heat uptake in CMIP5 models. *Journal of Climate* **28**(2), 862–886. doi:10.1175/JCLI-D-14-00117.1

Harrison, W. G., Harris, L. R., and Irwin, B. D. (1996). The kinetics of nitrogen utilization in the oceanic mixed layer: nitrate and ammonium interactions at nanomolar concentrations. *Limnology and Oceanography* **41**(1), 16–32. doi:10.4319/LO.1996.41.1.0016

Hassler, C. S., Ridgway, K. R., Bowie, A. R., Butler, E. C. V., Clementson, L. A., Doblin, M. A., Davies, D. M., Law, C., Ralph, P. J., van der Merwe, P., Watson, R., and Ellwood, M. J. (2014). Primary productivity induced by iron and nitrogen in the Tasman Sea: an overview of the PINTS expedition. *Marine and Freshwater Research* **65**(6), 517–537. doi:10.1071/MF13137

Herraiz-Borreguero, L., and Rintoul, S. R. (2011). Subantarctic mode water: distribution and circulation. *Ocean Dynamics* **61**(1), 103–126. doi:10.1007/S10236-010-0352-9

Hunter, K. A., and Boyd, P. (1999). Biogeochemistry of trace metals in the ocean. *Marine and Freshwater Research* **50**(8), 739–753. doi:10.1071/MF99070

Hutchins, D. A., Sedwick, P. N., DiTullio, G. R., Boyd, P. W., Quéguiner, B., Griffiths, F. B., and Crossley, C. (2001). Control of phytoplankton growth by iron and silicic acid availability in the subantarctic Southern

Ocean: experimental results from the SAZ Project. *Journal of Geophysical Research – Oceans* **106**, 31559–31572. doi:10.1029/2000JC000333

John, S. G., and Conway, T. M. (2014). A role for scavenging in the marine biogeochemical cycling of zinc and zinc isotopes. *Earth and Planetary Science Letters* **394**, 159–167. doi:10.1016/J.EPSL.2014.02.053

John, G. S., Geis, R. W., Saito, M. A., and Boyle, E. A. (2007). Zinc isotope fractionation during high-affinity and low-affinity zinc transport by the marine diatom *Thalassiosira oceanica*. *Limnology and Oceanography* **52**(6), 2710–2714. doi:10.4319/LO.2007.52.6.2710

Köbberich, M., and Vance, D. (2017). Kinetic control on Zn isotope signatures recorded in marine diatoms. *Geochimica et Cosmochimica Acta* **210**, 97–113. doi:10.1016/J.GCA.2017.04.014

Lourey, M. J., and Trull, T. W. (2001). Seasonal nutrient depletion and carbon export in the Subantarctic and Polar Frontal Zones of the Southern Ocean south of Australia. *Journal of Geophysical Research – Oceans* **106**, 31463–31487. doi:10.1029/2000JC000287

Marković, T., Manzoor, S., Humphreys-Williams, E., Kirk, G. J. D., Vilar, R., and Weiss, D. J. (2017). Experimental determination of zinc isotope fractionation in complexes with the phytosiderophore 2′-deoxymugeneic acid (DMA) and its structural analogues, and implications for plant uptake mechanisms. *Environmental Science & Technology* **51**(1), 98–107. doi:10.1021/ACS.EST.6B00566

Martin, J. H., Knauer, G. A., Karl, D. M., and Broenkow, W. W. (1987). VERTEX – carbon cycling in the northeast Pacific. *Deep-Sea Research – A. Oceanographic Research Papers* **34**(2), 267–285. doi:10.1016/0198-0149(87)90086-0

Mattinson, J. M. (1972). Preparations of hydrofluoric, hydrochloric and nitric acids at ultralow lead levels. *Analytical Chemistry* **44**(9), 1715–1716. doi:10.1021/AC60317A032

Metzl, N., Tilbrook, B., and Poisson, A. (1999). The annual fCO_2 cycle and the air–sea CO_2 flux in the sub-Antarctic Ocean. *Tellus – B. Chemical and Physical Meteorology* **51**(4), 849–861. doi:10.3402/TELLUSB.V51I4.16495

Moeller, K., Schoenberg, R., Pedersen, R.-B., Weiss, D., and Dong, S. (2012). Calibration of the new certified reference materials ERM-AE633 and ERM-AE647 for copper and IRMM-3702 for zinc isotope amount ratio determinations. *Geostandards and Geoanalytical Research* **36**(2), 177–199. doi:10.1111/J.1751-908X.2011.00153.X

Moreau, S., Penna, A. D., Llort, J., Patel, R., Langlais, C., Boyd, P. W., Matear, R. J., Phillips, H. E., Trull, T. W., Tilbrook, B., Lenton, A., and Strutton, P. G. (2017). Eddy-induced carbon transport across the Antarctic Circumpolar Current. *Global Biogeochemical Cycles* **31**(9), 1368–1386. doi:10.1002/2017GB005669

Oliver, E. C. J., and Holbrook, N. J. (2014). Extending our understanding of South Pacific gyre 'spin-up': modeling the East Australian Current in a future climate. *Journal of Geophysical Research – Oceans* **119**(5), 2788–2805. doi:10.1002/2013JC009591

Orsi, A. H., Whitworth, I. I. I. T., and Nowlin, J. W. D. (1995). On the meridional extent and fronts of the Antarctic Circumpolar Current. *Deep-sea Research – I. Oceanographic Research Papers* **42**(5), 641–673. doi:10.1016/0967-0637(95)00021-W

Paasche, E. (1973). Silicon and the ecology of marine plankton diatoms. I. *Thalassiosira pseudonana* (*Cyclotella nana*) grown in a chemostat with silicate as limiting nutrient. *Marine Biology* **19**(2), 117–126. doi:10.1007/BF00353582

Patel, R. S., Phillips, H. E., Strutton, P. G., Lenton, A., and Llort, J. (2019). Meridional heat and salt transport across the subantarctic front by cold-core eddies. *Journal of Geophysical Research – Oceans* **124**(2), 981–1004. doi:10.1029/2018JC014655

Petrou, K., Hassler, C. S., Doblin, M. A., Shelly, K., Schoemann, V., van den Enden, R., Wright, S., and Ralph, P. J. (2011). Iron-limitation and high light stress on phytoplankton populations from the Australian Sub-Antarctic Zone (SAZ). *Deep-sea Research – II. Topical Studies in Oceanography* **58**(21–22), 2200–2211. doi:10.1016/J.DSR2.2011.05.020

Poitrasson, F., and Freydier, R. (2005). Heavy iron isotope composition of granites determined by high resolution MC-ICP-MS. *Chemical Geology* **222**(1–2), 132–147. doi:10.1016/J.CHEMGEO.2005.07.005

Raimbault, P., and Garcia, N. (2008). Evidence for efficient regenerated production and dinitrogen fixation in nitrogen-deficient waters of the South Pacific Ocean: impact on new and export production estimates. *Biogeosciences* **5**(2), 323–338. doi:10.5194/BG-5-323-2008

Raven, J. A. (2013). The evolution of autotrophy in relation to phosphorus requirement. *Journal of Experimental Botany* **64**(13), 4023–4046. doi:10.1093/JXB/ERT306

Ridgway, K. R. (2007). Seasonal circulation around Tasmania: an interface between eastern and western boundary dynamics. *Journal of Geophysical Research* **112**, C10016. doi:10.1029/2006JC003898

Rintoul, S. R., and Trull, T. W. (2001). Seasonal evolution of the mixed layer in the Subantarctic Zone south of Australia. *Journal of Geophysical Research – Oceans* **106**, 31447–31462. doi:10.1029/2000JC000329

Roshan, S., DeVries, T., Wu, J., and Chen, G. (2018). The internal cycling of zinc in the ocean. *Global Biogeochemical Cycles* **32**, 1833–1849. doi:10.1029/2018GB006045

Sallée, J. B., Wienders, N., Speer, K., and Morrow, R. (2006). Formation of subantarctic mode water in the southeastern Indian Ocean. *Ocean Dynamics* **56**(5–6), 525–542. doi:10.1007/S10236-005-0054-X

Samanta, M., Ellwood, M. J., and Mortimer, G. E. (2016). A method for determining the isotopic composition of dissolved zinc in seawater by MC-ICP-MS with a ^{67}Zn–^{68}Zn double spike. *Microchemical Journal* **126**, 530–537. doi:10.1016/J.MICROC.2016.01.014

Samanta, M., Ellwood, M. J., Sinoir, M., and Hassler, C. S. (2017). Dissolved zinc isotope cycling in the Tasman Sea, SW Pacific Ocean. *Marine Chemistry* **192**, 1–12. doi:10.1016/J.MARCHEM.2017.03.004

Samanta, M., Ellwood, M. J., and Strzepek, R. F. (2018). Zinc isotope fractionation by *Emiliania huxleyi* cultured across a range of free zinc ion concentrations. *Limnology and Oceanography* **63**, 660–671. doi:10.1002/LNO.10658

Sarmiento, J. L., Gruber, N., Brzezinski, M. A., and Dunne, J. P. (2004). High-latitude controls of thermocline nutrients and low latitude biological productivity. *Nature* **427**, 56–60. [Published erratum appears in *Nature* **2011**, 479, 556]. doi:10.1038/NATURE02127

Schlosser, C., Klar, J. K., Wake, B. D., Snow, J. T., Honey, D. J., Woodward, E. M. S., Lohan, M. C., Achterberg, E. P., and Moore, C. M. (2014). Seasonal ITCZ migration dynamically controls the location of the (sub)tropical Atlantic biogeochemical divide. *Proceedings of the National Academy of Sciences of the United States of America* **111**(4), 1438–1442. doi:10.1073/PNAS.1318670111

Sedwick, P. N., DiTullio, G. R., Hutchins, D. A., Boyd, P. W., Griffiths, F. B., Crossley, A. C., Trull, T. W., and Queguiner, B. (1999). Limitation of algal growth by iron deficiency in the Australian Subantarctic region. *Geophysical Research Letters* **26**(18), 2865–2868. doi:10.1029/1998GL002284

Shadwick, E. H., Trull, T. W., Tilbrook, B., Sutton, A. J., Schulz, E., and Sabine, C. L. (2015). Seasonality of biological and physical controls on surface ocean CO_2 from hourly observations at the Southern Ocean Time Series site south of Australia. *Global Biogeochemical Cycles* **29**(2), 223–238. doi:10.1002/2014GB004906

Speer, K., Rintoul, S. R., and Sloyan, B. (2000). The diabatic deacon cell. *Journal of Physical Oceanography* **30**(12), 3212–3222. doi:10.1175/1520-0485(2000)030<3212:TDDC>2.0.CO;2

Strzepek, R. F., Hunter, K. A., Frew, R. D., Harrison, P. J., and Boyd, P. W. (2012). Iron–light interactions differ in Southern Ocean phytoplankton. *Limnology and Oceanography* **57**(4), 1182–1200. doi:10.4319/LO.2012.57.4.1182

Sunda, W. G., and Huntsman, S. A. (1992). Feedback interactions between zinc and phytoplankton in seawater. *Limnology and Oceanography* **37**(1), 25–40. doi:10.4319/LO.1992.37.1.0025

Tagliabue, A., Sallée, J.-B., Bowie, A. R., Levy, M., Swart, S., and Boyd, P. W. (2014). Surface-water iron supplies in the Southern Ocean

sustained by deep winter mixing. *Nature Geoscience* **7**(4), 314–320. doi:10.1038/NGEO2101

Thompson, C. M., and Ellwood, M. J. (2014). Dissolved copper isotope biogeochemistry in the Tasman Sea, SW Pacific Ocean. *Marine Chemistry* **165**, 1–9. doi:10.1016/J.MARCHEM.2014.06.009

Trull, T., Rintoul, S. R., Hadfield, M., and Abraham, E. R. (2001*a*). Circulation and seasonal evolution of polar waters south of Australia: implications for iron fertilization of the Southern Ocean. *Deep-sea Research – II. Topical Studies in Oceanography* **48**(11–12), 2439–2466. doi:10.1016/S0967-0645(01)00003-0

Trull, T. W., Bray, S. G., Manganini, S. J., Honjo, S., and Francois, R. (2001*b*Moored sediment trap measurements of carbon export in the Subantarctic and Polar Frontal Zones of the Southern Ocean, south of Australia. *Journal of Geophysical Research – Oceans* **106**, 31489–31509. doi:10.1029/2000JC000308

Twining, B. S., Nodder, S. D., King, A. L., Hutchins, D. A., LeCleir, G. R., DeBruyn, J. M., Maas, E. W., Vogt, S., Wilhelm, S. W., and Boyd, P. W. (2014). Differential remineralization of major and trace elements in sinking diatoms *Limnology and Oceanography* **59**(3), 689–704. doi:10.4319/LO.2014.59.3.0689

Vance, D., Little, S. H., de Souza, G. F., Khatiwala, S., Lohan, M. C., and Middag, R. (2017). Silicon and zinc biogeochemical cycles coupled through the Southern Ocean. *Nature Geoscience* **10**, 202–206. doi:10.1038/NGEO2890

Wang, R. M., Archer, C., Bowie, A. R., and Vance, D. (2018). Zinc and nickel isotopes in seawater from the Indian Sector of the Southern Ocean: the impact of natural iron fertilization versus Southern Ocean hydrography and biogeochemistry. *Chemical Geology* **12**, 12–34.

Weber, T., John, S., Tagliabue, A., and DeVries, T. (2018). Biological uptake and reversible scavenging of zinc in the global ocean. *Science* **361** (6397), 72–76. doi:10.1126/SCIENCE.AAP8532

Weeding, B., and Trull, T. W. (2014). Hourly oxygen and total gas tension measurements at the Southern Ocean Time Series site reveal winter ventilation and spring net community production. *Journal of Geophysical Research – Oceans* **119**(1), 348–358. doi:10.1002/2013JC009302

Westwood, K. J., Brian Griffiths, F., Webb, J. P., and Wright, S. W. (2011). Primary production in the Sub-Antarctic and Polar Frontal Zones south of Tasmania, Australia; SAZ-Sense survey, 2007. *Deep-sea Research – II. Topical Studies in Oceanography* **58**(21–22), 2162–2178. doi:10.1016/J.DSR2.2011.05.017

Wood, E. D., Armstrong, F. A. J., and Richards, F. A. (1967). Determination of nitrate in sea water by cadmium-copper reduction to nitrite. *Journal of the Marine Biological Association of the United Kingdom* **47**(1), 23–31. doi:10.1017/S002531540003352X

Handling Editor: Max Finlayson